Overview of DFIG-Based Wind Power System Resonances Under Weak Networks

Yipeng Song, *Member, IEEE*, and Frede Blaabjerg, *Fellow, IEEE*

***Abstract*—The wind power generation techniques are continuing to develop and increasing numbers of doubly fed induction generator (DFIG)-based wind power systems are connecting to the on-shore and off-shore grids, local standalone weak networks, and microgrid applications. The impedances of the weak networks are too large to be neglected and require careful attention. Due to the impedance interaction between the weak network and the DFIG system, both subsynchronous resonance (SSR) and high-frequency resonance (HFR) may occur when the DFIG system is connected to the series or parallel compensated weak network. This paper will discuss the SSR and the HFR phenomena based on the impedance modeling of the DFIG system and the weak networks, and the cause of these two resonances will be explained in details. The following factors will be discussed in this paper: 1) transformer configuration; 2) different power scale of DFIG system with different parameters; 3) *L* or *LCL* filter adopted in the grid side converter (GSC); 4) rotor speed; 5) current closed-loop controller parameters; and 6) digital control delay. On the basis of the analysis, active damping strategies for HFR using virtual impedance concept will be proposed.**

***Index Terms*—Active damping, doubly fed induction generator (DFIG) system impedance, high-frequency resonance (HFR), subsynchronous resonance (SSR), weak network impedance.**

I. INTRODUCTION

THE demand for renewable power generation has been continually increasing in the past decades, and there have been two popular renewable power generation solutions worldwide in a large scale, i.e., the photovoltaic based solar energy and wind turbine-based wind power [1]–[5].

Several different topologies and generators of wind power generation have been under commercial development and operation for years, i.e., doubly fed induction generator (DFIG)-based wind power generation [6]–[18], permanent-magnet synchronous generator (PMSG) based wind power generation [19]–[24], and squirrel cage induction generator (SCIG) based wind power generation [25]. The topology differences between these three wind power systems are that the back-to-back pulsewidth-modulated (PWM) converters are connected between the PMSG/SCIG and the power network, while it is connected between the rotor side converter (RSC) and the grid side converter (GSC) in the DFIG system, and the DFIG stator winding is directly connected to the power network. This difference determines that the PMSG- and SCIG-based systems are less sensitive to the power network variation than the DFIG-based system. For instance, an appropriate control strategy of both PWM converters can ensure satisfactory low-voltage ride-through (LVRT) performance of the PMSG and SCIG systems [19] and also provide excellent rejection capability against the grid voltage unbalance, distortion, and disturbance [20]. Moreover, a well-regulated constant dc-link voltage ensures a decoupled control of the two PWM converters, and thus, the impedance interaction between the generators (PMSG/SCIG) and the power network may be less likely to exist.

Unfortunately, due to the direct connection of the stator winding to the power network, the DFIG-based wind power system is comparatively more sensitive to the power network variation, including voltage unbalance [6]–[10], low voltage fault [11]–[14], distortion [15]–[18], and potential resonance due to a comparatively large impedance of the weak network.

There are mainly two kinds of resonances in the DFIG system, i.e., the subsynchronous resonance (SSR) below the fundamental frequency when connected to the series compensated weak network [29]–[46] and the high-frequency resonance (HFR) when connected to the parallel compensated weak network [26]–[28].

Due to the impedance interaction between the DFIG system and the series compensated weak network, the SSR [29]–[46] may occur and even result in instability operation in the DFIG system. The harmonic linearization method was employed to obtain the positive and negative impedance of the DFIG system in [29] and [30], and then the frequency of SSR can be analyzed based on the obtained impedance modeling. Miao [31] gave out a comprehensive impedance modeling of the DFIG system under series compensated network, but the GSC is neglected. Thyristor-controlled and gate-controlled series capacitors are demonstrated, respectively, in [32] and [33] to reshape the network impedance, thereby avoiding the potential SSR. Fan and Miao [34] adopted the impedance-based Nyquist stability criterion in order to explain the SSR phenomenon. An eigenvalue-based analysis was conducted in [35] to investigate the impact of SSR from the perspective of the grid and the DFIG. Three different modal resonances were also analyzed in [36]–[38], i.e., induction generator effect, torsional interactions, and control interactions. The SSR was analyzed from the quantitative perspective using an aggregated *RLC* circuit model of the series compensated weak network in [39].

Manuscript received June 11, 2016; revised July 27, 2016; accepted August 16, 2016. Date of publication August 19, 2016; date of current version February 11, 2017. Recommended for publication by Associate Editor Pavol Bauer.

The authors are with the Department of Energy Technology, Aalborg University, Aalborg 9220, Denmark (e-mail: yis@et.aau.dk; fbl@et.aau.dk).

Color versions of one or more of the figures in this paper are available online at http://ieeexplore.ieee.org.

Digital Object Identifier 10.1109/TPEL.2016.2601643

Based on the SSR theoretical analysis, several damping strategies have been developed to mitigate the SSR. The phase margin can be successfully increased by inserting a virtual resistance in [40] and the resonance can be mitigated consequently. An auxiliary SSR damping controller with the selection of control signals in the DFIG converters was proposed in [41] to effectively mitigate the SSR. Moreover, by choosing properly an optimum input control signal, a simple proportional SSR damping controller for the RSC and GSC was designed to mitigate the SSR in [42]. A multi-input, multi-output state-space methodology was proposed in [43] based on the DFIG stator and rotor current feedback to damp the SSR. A two-degree-of-freedom control strategy was introduced to mitigate the SSR in [44], while the supplementary damping control was designed to damp the SSR in the DFIG system in [45]. An overview paper regarding SSR active damping strategy was summarized in [46], which includes the thyristor-controlled series capacitor, gate-controlled series capacitor, and GSC control.

Besides the SSR, which is a low-frequency resonance below the fundamental frequency, the HFR is also likely to occur, especially in the grid-connected converters [47]–[62]. Many effective damping strategies for the HFR in the grid-connected converters have been reported in [47]–[53]. The active damping of harmonic distortion in the grid-connected converter has been well investigated in [47]–[51]. The output impedance shaping attained by the virtual impedances is generalized using the impedance-based models in [51], with different virtual impedances configuration and their implementation issues discussed. The current controller parameters are optimally designed to improve its stability under a weak network [54], [55]. Also, the digital control delay is investigated and mitigated in [56] and [57] in order to improve the converter performance. An impedance modeling approach of the three-phase grid-connected converters is also established in *d*—*q* reference frame [59], [60] to analyze its stability issue.

Based on the aforementioned overview, it might be likely that the HFR may occur if the DFIG system is connected to the parallel compensated weak network [26]–[28]. The following variables may influence the HFR phenomenon: 1) transformer configuration between the DFIG machine stator winding, the grid side output filter, and the point of common coupling (PCC); 2) different power-scale DFIG system having different parameters, which may vary from several kilowatts to several megawatts; 3) different *L* or *LCL* filters adopted in the GSC; 4) rotor speed of subsynchronous speed or supersynchronous speed; 5) current closed-loop controllers proportional and integral parameters; and 6) digital control delay caused by the voltage and current sampling as well as the PWM update in the control system.

It is important to point out that, since the SSR has been well investigated in the previous works [29]–[46], the major contribution of this paper is to theoretically explain the HFR and its active damping, while the conclusions regarding the SSR will also be addressed and discussed in comparison with the HFR.

Based on the theoretical analysis, the active damping strategies for the aforementioned two resonances need to be introduced to mitigate the resonances, by reshaping the impedance of either the DFIG system or the weak network. During the impedance reshaping, the phase difference between the DFIG system and the weak networks at the potential resonance frequency needs to be reduced and the resonance can as a result be mitigated. Nevertheless, it should be pointed out that the active damping strategy based on the introduction of virtual impedance is only appropriate for the HFR damping (the reason will be explained in following discussion); thus, only the active damping of the HFR, but not the active damping of the SSR, will be discussed in this paper.

This paper introduces first the impedance modeling of the DFIG system in Section II, including the rotor part of the DFIG machine and the RSC and the grid part of the *L*/*LCL* filter and the GSC. Then, the reasons for causing the SSR and HFR are theoretically analyzed and explained based on the established impedance modeling in Section III. It is pointed out that both resonances are caused by the impedance interaction between the DFIG system and the weak network. Several influence factors as mentioned earlier will all be investigated in respect to the SSR and HFR in Section IV. The active damping strategy for the HFR based on the introduction of the virtual impedance is discussed in Section V. Simulation results and experimental results are provided to validate the theoretical analysis regarding the SSR and HFR in Section VI. Finally, the conclusions are summarized in Section VII.

II. IMPEDANCE MODELING OF THE DFIG SYSTEM

As an analysis platform for the DFIG system resonances, an impedance modeling of the DFIG system needs to be established first. Note that the impedance modeling of the DFIG system has been reported in [31], and a detailed description of the DFIG system modeling is mentioned in this section.

A. Description of the DFIG System and Weak Network

A configuration diagram of the investigated DFIG system is given in Fig. 1. As it can be seen from Fig. 1, the RSC performs effective control of the DFIG stator output power through the rotor current control, the GSC keeps a constant and stable dc-link voltage, and either *LCL* filter [11]–[13] or *L* filter [6]–[10], [14]–[18] can be adopted to filter out the switching harmonics.

A three-terminal step-up transformer is always connected between the DFIG machine stator winding, the GSC output *LCL* filter, and the PCC to increase the voltage level of the DFIG system. On the other hand, the three alternative configurations of weak networks will be considered in this paper: 1) noncompensated network, with the network resistance R_{NET} and network inductance L_{NET} connected in series; 2) the series compensated network, with the R_{NET}, L_{NET}, and network capacitance C_{NET} connected in series; 3) the parallel compensated network, with the R_{NET} and L_{NET} connected in series and the C_{NET} connected in parallel. Besides, a two-terminal transformer is always adopted to adjust the voltage level between the PCC and the high-voltage long-distance transmission cables.

B. Impedance Modeling of the GSC and L/LCL Filter

The impedance modeling of the GSC with *L* filter is investigated and obtained in [31], as shown in Fig. 2. A similar

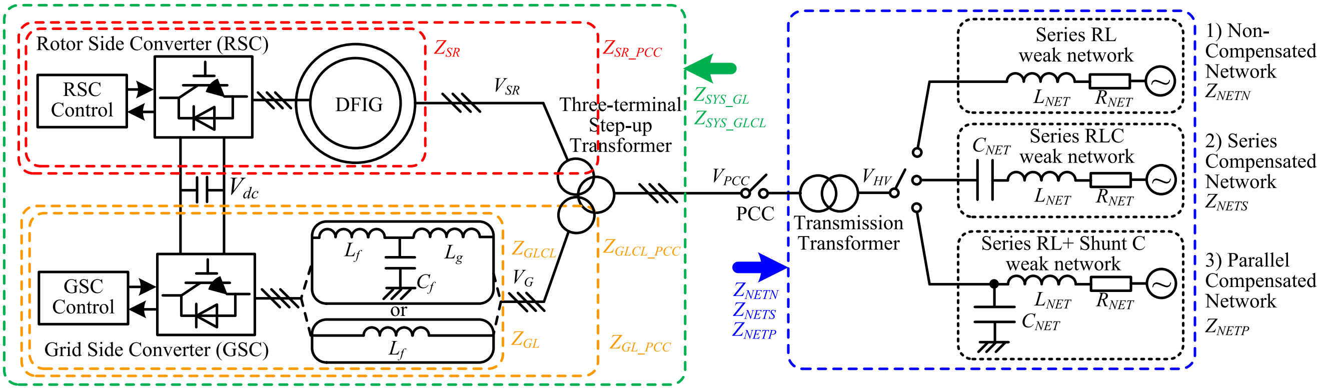

Fig. 1. Configuration of the DFIG system and its connection to the weak network.

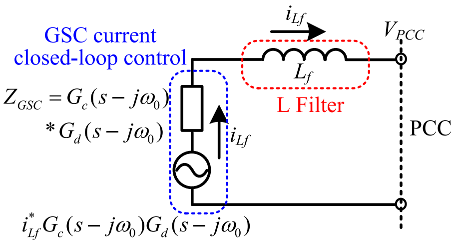

Fig. 2. Impedance modeling of the GSC equipped with L filter.

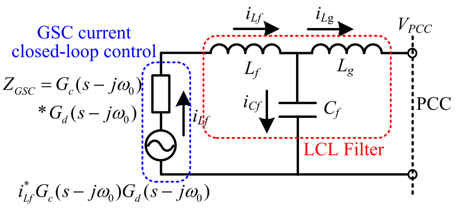

Fig. 3. Impedance modeling of GSC equipped with *LCL* filter.

impedance modeling of the GSC with *LCL* filter can be obtained, as shown in Fig. 3. Note that the voltage level increasing caused by the transformer is not included in this impedance modeling, but it will be discussed in the following analysis.

The GSC current closed-loop control is modeled as one voltage source $i^* \; LfG_c(s - j\omega_0)G_d(s - j\omega_0)$ and one impedance $Z_{\mathrm{GSC}} = G_c(s - j\omega_0)G_d(s - j\omega_0)$ in series, as shown in the blue bracket in Figs. 2 and 3. $G_c(s - j\omega_0)$ is the PI current controller containing proportional part K_{pgsc} and integral part $K_{\mathrm{igsc}}/(s - j\omega_0)$, the parameters of K_{pgsc} and K_{igsc} can be found in Tables I and II. $G_d(s - j\omega_0)$ is the digital control delay of 1.5 sample period due to the delay of sampling and PWM update [51]. It needs to be pointed out that ω_0 is the grid fundamental component angular speed of 100π rad/s. The introduction of ω_0 is due to the reference frame rotation from the stationary frame to the synchronous frame where the PI closed-loop current regulation is implemented. The control loop of the dc-link voltage and the grid synchronization in the GSC are neglected due to the slower dynamic response [31].

Then, based on Fig. 3, the impedance of the GSC and *L*/*LCL* filter can be obtained by setting the voltage source to zero

$$Z_{\mathrm{GL}} = Z_{L_f} + Z_{\mathrm{GSC}} \tag{1a}$$

$$Z_{\mathrm{GLCL}} = \frac{Z_{C_f}\left(Z_{L_f} + Z_{\mathrm{GSC}}\right) + Z_{L_g}\left(Z_{L_f} + Z_{\mathrm{GSC}}\right) + Z_{C_f}Z_{L_g}}{Z_{C_f} + \left(Z_{L_f} + Z_{\mathrm{GSC}}\right)} \tag{1b}$$

where C_f is the *LCL* capacitor filter, L_f and L_g are the *LCL* inductor filters close to the converter and grid, respectively, $Z_{\mathrm{GSC}} = G_c(s - j\omega_0)G_d(s - j\omega_0)$,$Z_{Cf} = 1/sC_f$, $Z_{Lf} = sL_f$, $Z_{Lg} = sL_g$.

TABLE I
PARAMETERS OF SMALL-SCALE 7.5 KW DFIG SYSTEM

DFIG Machine			
Rated Power	7.5 kW	T_d	150 μs
R_s	0.44 Ω	R_r	0.64 Ω
$L_{\sigma s}$	3.44 mH	$L_{\sigma r}$	5.16 mH
L_m	79.3 mH	Pole Pairs	3
f_s	10 kHz	f_{sw}	5 kHz
LCL Filter			
L_g	7 mH	L_f	11 mH
C_f	6.6 uF		
L Filter			
L_f	11 mH		
Voltage Level and Ratios			
V_{SR}	400 V	V_G	400 V
V_{PCC}	400 V		
K_1	1	K_2	1
Current Controller Parameters			
K_{prsc}	8	K_{irsc}	16
K_{pgsc}	8	K_{igsc}	16

C. Impedance Modeling of the DFIG Machine and RSC

According to [31], the impedance modeling of the DFIG machine and RSC can be obtained, as shown in Fig. 4. Similarly, the voltage level increase caused by the transformer is not included here but will be discussed later.

Since the rotor current control is implemented in the synchronous reference frame, it needs to be transformed into the rotor stationary frame using the slip angular speed expressed

TABLE II
PARAMETERS OF LARGE-SCALE 2.0 MW DFIG SYSTEM

DFIG Machine			
Rated Power	2.0 MW	T_d	300 μs
R_s	0.0015 Ω	R_r	0.0016 Ω
$L_{\sigma s}$	0.04 mH	$L_{\sigma r}$	0.06 mH
L_m	3 mH	Pole Pairs	3
f_s	5 kHz	f_{sw}	2.5 kHz
LCL Filter			
L_g	125 μH	L_f	125 μH
C_f	220 μF		
L Filter			
L_f	125 μH		
Voltage Level and Ratios			
V_G	480 V	V_{SR}	690 V
V_{PCC}	1 kV		
K_1	2.08	K_2	1.45
Current Controller Parameters			
K_{prsc}	0.2	K_{irsc}	2
K_{pgsc}	0.05	K_{igsc}	2

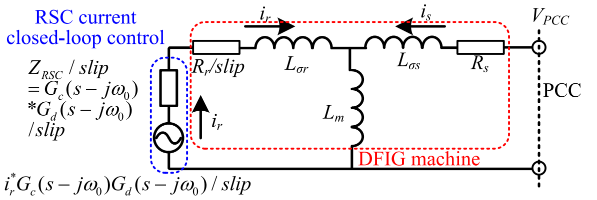

Fig. 4. Impedance modeling of the DFIG machine and RSC.

as [29]–[31]

$$\text{slip} = (s - j\omega_r)/s \tag{2}$$

where ω_r is the rotor angular speed.

Then, the impedance of the DFIG machine and RSC can be obtained by setting the rotor control voltage source to zero, and the impedance of the DFIG machine and RSC can be presented as [31]

$$Z_{\mathrm{SR}} = \frac{Z_{L_m} H + (R_s + Z_{L_{\sigma s}}) H + Z_{L_m} (R_s + Z_{L_{\sigma s}})}{Z_{L_m} + H} \tag{3}$$

where $H = Z_{L\sigma r} + (R_r + Z_{\mathrm{RSC}})/\text{slip}$, $Z_{Lm} = sL_m$; $Z_{L\sigma r} = sL_{\sigma r}$; $Z_{L\sigma s} = sL_{\sigma s}$; R_r and R_s are the rotor and stator winding resistances; $L_{\sigma r}$ and $L_{\sigma s}$ are the rotor and stator leakage inductances, respectively; L_m is the mutual inductance; and $Z_{\mathrm{RSC}} = G_c(s - j\omega_0) G_d(s - j\omega_0)$.

D. Impedance Modeling of the Three-Terminal Transformer

In the aforementioned two impedance modeling (1) and (3), the three-terminal step-up transformer is not included. However, it is always adopted to increase the voltage level between the DFIG system and PCC in the commercial DFIG system. For instance, for a commercial 2.0 MW DFIG system, the stator voltage is normally 690 V and, *LCL* filter output voltage is 480 V, and the PCC voltage is 1 kV. Thus, the influence of the transformer on the impedance modeling needs to be taken into consideration.

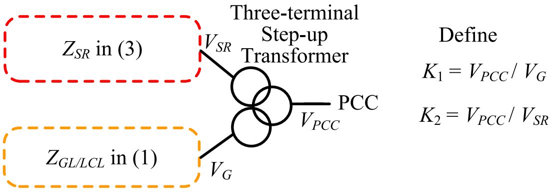

Fig. 5. Simplified DFIG system configuration diagram with a step-up transformer.

Fig. 5 shows the simplified configuration diagram of the DFIG system. The voltage transformer turns ratios between the primary side and the secondary side are defined as

$$K_1 = V_{\mathrm{PCC}}/V_G \tag{4a}$$

$$K_2 = V_{\mathrm{PCC}}/V_{\mathrm{SR}}. \tag{4b}$$

Then, based on (1) and (4), the impedance $Z_{\mathrm{GL\_PCC}}$/$Z_{\mathrm{GLCL\_PCC}}$ of the GSC and *L*/*LCL* filter seen from the PCC can be presented as

$$Z_{GL\_\mathrm{PCC}} = K_1^2 \left(Z_{L_f} + Z_{\mathrm{GSC}}\right) \tag{5a}$$

$$Z_{\mathrm{GLCL\_PCC}} = K_1^2 \frac{Z_{C_f}\left(Z_{L_f} + Z_{\mathrm{GSC}}\right) + Z_{L_g}\left(Z_{L_f} + Z_{\mathrm{GSC}}\right) + Z_{C_f} Z_{L_g}}{Z_{C_f} + \left(Z_{L_f} + Z_{\mathrm{GSC}}\right)}. \tag{5b}$$

Similarly, based on (3) and (4), the impedance Z_{SR_PCC} of the DFIG and RSC seen from the PCC can be presented as

$$Z_{SR\_\mathrm{PCC}} = K_2^2 \frac{Z_{L_m} H + (R_s + Z_{L_{\sigma s}}) H + Z_{L_m} (R_s + Z_{L_{\sigma s}})}{Z_{L_m} + H}. \tag{6}$$

E. Impedance Modeling of the DFIG System

According to Fig. 1, the dc-link capacitor is connected between RSC and GSC and the dc-link voltage is able to remain constant in normal operation; thus, the dc-link capacitor actually has the function to decouple the control of the RSC and GSC. As a result, the RSC and GSC can work independently, and no dc-link coupling between RSC and GSC needs to be taken into consideration in the impedance modeling. Therefore, the rotor part (RSC and DFIG) and the grid part (GSC and *LCL* filter) can be regarded as in parallel connection to the PCC via the three-terminal transformer.

Based on the impedance modeling of the GSC and *L*/*LCL* filter in (5), the DFIG and RSC in (6), as well as the three-terminal transformer in (4), the DFIG system impedance modeling seen from the PCC can be obtained as

$$Z_{\mathrm{SYS\_GL}} = \frac{Z_{GL\_\mathrm{PCC}} Z_{SR\_\mathrm{PCC}}}{Z_{GL\_\mathrm{PCC}} + Z_{SR\_\mathrm{PCC}}} \tag{7a}$$

$$Z_{\mathrm{SYS\_GLCL}} = \frac{Z_{\mathrm{GLCL\_PCC}} Z_{SR\_\mathrm{PCC}}}{Z_{\mathrm{GLCL\_PCC}} + Z_{SR\_\mathrm{PCC}}}. \tag{7b}$$

The impedance modeling discussed earlier are applicable for both small- and large-power-scale DFIG system.

F. Impedance Modeling of the Weak Networks

As an important role of the resonance phenomenon in the DFIG system, the impedance modeling of the weak networks needs to be established. The weak network configuration is becoming increasingly complicated nowadays with a large number of various power sources and loads. Any connection or disconnection of sources and loads will result in impedance change of the weak network. However, for any types of sources and loads, their impedance can be equivalently presented as the combinations of basic units of *R*, *L*, *C*. Therefore, it is possible to merge several sources and loads impedance into one equivalent impedance. For instance, in the SSR discussion, it is assumed that the equivalent impedance of the series compensated weak network is *R*, *L*, and *C* in series connection [29]–[46]; similarly, in the HFR discussion, it is assumed that the equivalent impedance of the parallel compensated weak network is *R* and *L* in series connection and *C* in parallel connection [26]–[28].

For the parallel compensated weak network, shunt (parallel) capacitors are commonly used as static reactive power compensation with the purpose to achieve high power factor in the off-shore wind farms [1]–[4]. Furthermore, in the case of the cable-based weak network, the parasitic capacitances between the transmission cables and grounds [5] are also inevitable and can vary greatly in practical situations. Thus, it can be found out that the presence of shunt (parallel) capacitor is a reasonable assumption for the parallel compensated weak network when discussing the DFIG system HFR issues.

For the series compensated weak network, the series compensated capacitance is always connected in series with the transmission cables to reduce the electric length of the transmission cable and increase the power transmission capability. In [29]–[46], the series compensated weak network has the typical configuration of *R, L*, and *C* in series connection.

In a practical wind farm, the transmission transformer is always connected between the voltage at PCC ($V_{\mathrm{PCC}} = 1\,\mathrm{kV}$) and the high-voltage long-distance transmission cable ($V_{\mathrm{HV}} =$ 25 kV, note that this voltage level may change in different countries and that the value here is just taken as an example). As a consequence, all the network parameters R_{NET}, L_{NET}, and C_{NET} in the high-voltage long-distance transmission cable should include the voltage turns ratio as

$$K_3 = V_{\mathrm{HV}}/V_{\mathrm{PCC}}. \tag{8}$$

Thus, based on Fig. 1 and (8), the impedance of the three weak networks configurations seen from PCC can be presented as [26]–[31]

$$Z_{\mathrm{NETN}} = sL_{\mathrm{NETN}}/K_3^2 + R_{\mathrm{NETN}}/K_3^2 \tag{9a}$$

$$Z_{\mathrm{NETS}} = sL_{\mathrm{NETS}}/K_3^2 + R_{\mathrm{NETS}}/K_3^2 + \frac{1}{sK_3^2 C_{\mathrm{NETS}}} \tag{9b}$$

$$Z_{\mathrm{NETP}} = \frac{\left(sL_{\mathrm{NETP}}/K_3^2 + R_{\mathrm{NETP}}/K_3^2\right)\frac{1}{sK_3^2 C_{\mathrm{NETP}}}}{sL_{\mathrm{NETP}}/K_3^2 + R_{\mathrm{NETP}}/K_3^2 + \frac{1}{sK_3^2 C_{\mathrm{NETP}}}} \tag{9c}$$

where Z_{NET} is the impedance of the weak network seen from the PCC, with subscripts N, S, and P representing the noncompensation, series compensation, and parallel compensation, respectively. R_{NET}, L_{NET} and C_{NET} are the network resistance, inductance and capacitance respectively in the high-voltage long-distance transmission cable.

III. ANALYSIS OF HFR AND SSR

Based on the DFIG system impedance modeling in the previous section, the HFR and SSR phenomena of the DFIG system will be analyzed with the consideration of the following several critical factors: 1) different power scale varying from kilowatts to megawatts; 2) *L* or *LCL* filter adopted in the GSC; 3) current closed-loop controller proportional and integral parameters; 4) rotor speed; and 5) digital control delay. Note that the issue of different transformer configurations has been discussed in previous section, so it will not be repeated here.

A. Impedance Shape of the DFIG Systems With Different Power Scale

According to (1) and (3), it can be found that the DFIG system parameters are involved in the impedance expression. Thus, the DFIG system with different power scale (varying from kilowatts to megawatts) will have a quite different impedance shape due to parameter variations of 10 to 100 times; this means the potential resonance frequency will vary a lot as a consequence.

In this paper, two different power-scale DFIG systems will be investigated, i.e., a small-scale 7.5 kW experimental DFIG setup and a large-scale 2.0 MW commercial DFIG setup, and their parameters are listed in Tables I and II, respectively.

According to Tables I and II, as the DFIG system power scale increases from 7.5 kW to 2.0 MW, the parameters of the DFIG machine stator/rotor resistance and inductance, as well as the *LCL* filter become 100 times smaller. Besides, the sampling frequency f_s and switching frequency f_{sw} also decrease from $f_s = 10$ kHz and $f_{\mathrm{sw}} = 5$ kHz for the small-scale DFIG system to $f_s = 5$ kHz and $f_{\mathrm{sw}} = 2.5$ kHz for the large-scale DFIG system. The proportional and integral parameters of the controllers K_p and K_i are also becoming much smaller, for instance, $K_{\mathrm{prsc}} = 8$, $K_{\mathrm{irsc}} = 16$ for the small-scale DFIG system, while $K_{\mathrm{prsc}} = 0.2$, $K_{\mathrm{irsc}} = 2$ for the large-scale DFIG system. All these parameter variations due to the different power scale will be taken into consideration in the following resonance analysis.

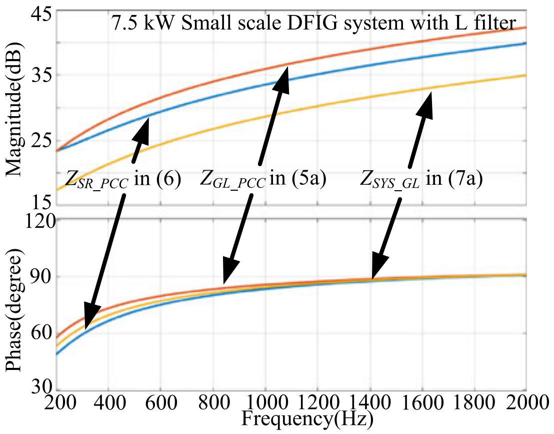

Fig. 6. Bode diagrams of small-scale DFIG system with *L* filter in the high-frequency range.

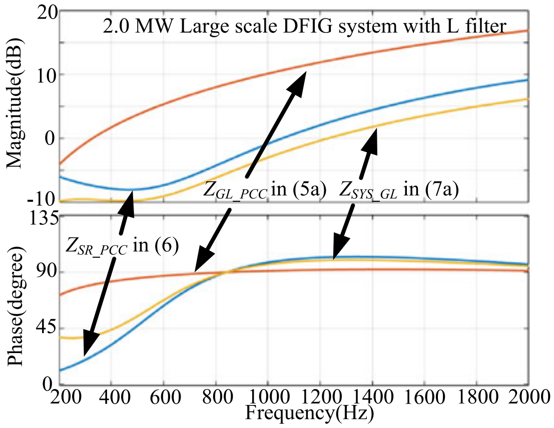

Fig. 8. Bode diagrams of large-scale DFIG system with *L* filter in the high-frequency range.

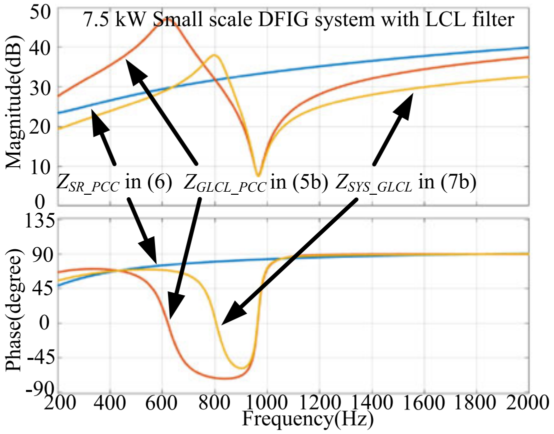

Fig. 7. Bode diagrams of small-scale DFIG system with *LCL* filter in the high-frequency range.

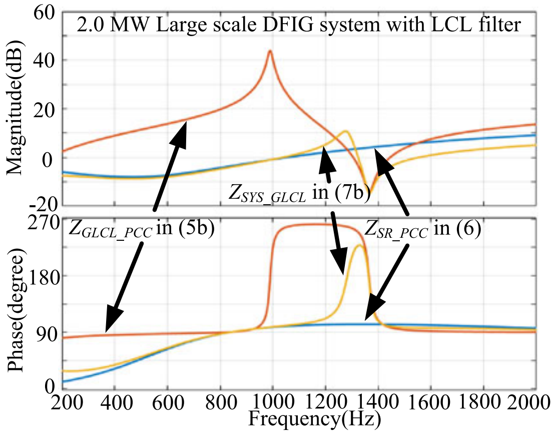

Fig. 9. Bode diagrams of large-scale DFIG system with *LCL* filter in the high-frequency range.

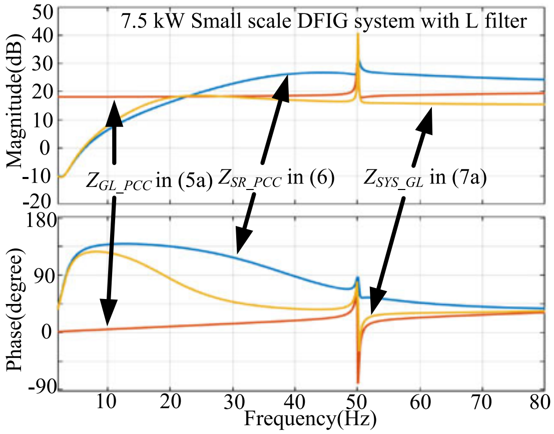

Fig. 10. Bode diagrams of small-scale DFIG system with *L* filter in the low-frequency range.

1) DFIG System Impedance in the High-Frequency Range: In respect to HFR, the impedance shape of both small- and large-power-scale DFIG system with *LCL* and *L* filters in the high-frequency range can be seen in Figs. 6–9. By analyzing the four Bode diagrams, it can be found that the DFIG system impedance shape has a magnitude concave and phase response changing of around 160° in Figs. 7 and 9 due to the adopted *LCL* filter. In contrast, when the *L* filter is adopted in GSC, the DFIG system impedance remains almost inductive within the high-frequency range, as shown in Figs. 6 and 8.

On the other hand, by comparing the Bode diagrams between the small-scale and large-scale DFIG systems, it can be observed that, since the parameters of the small-scale DFIG system in Table I is much larger than the parameters of the large-scale DFIG system in Table II, the impedance magnitude of the small-scale DFIG system in Figs. 6 and 7 is larger than the large-scale DFIG system shown in Figs. 8 and 9.

2) DFIG System Impedance in the Low-Frequency Range: Regarding the SSR phenomenon, the grid part impedance is always neglected in [29]–[31] due to the comparatively larger magnitude of the grid part compared to the rotor part. However, in this paper, for the sake of precise theoretical analysis, the grid part of the DFIG system is also taken into consideration, with the DFIG system impedance expression given in (5)–(7). The Bode diagram of both small- and large-power-scale DFIG systems in the low-frequency range in respect to the SSR is shown in Figs. 10–13.

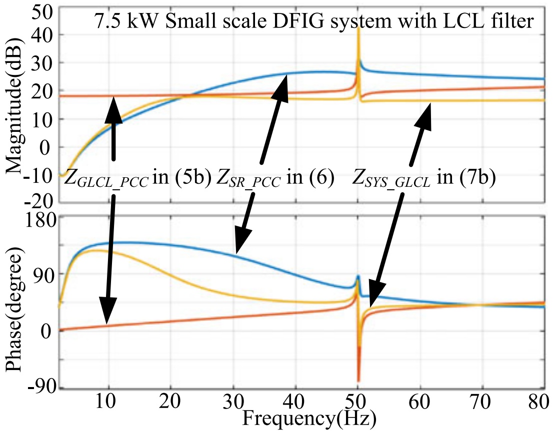

Fig. 11. Bode diagrams of small-scale DFIG system with *LCL* filter in the low-frequency range.

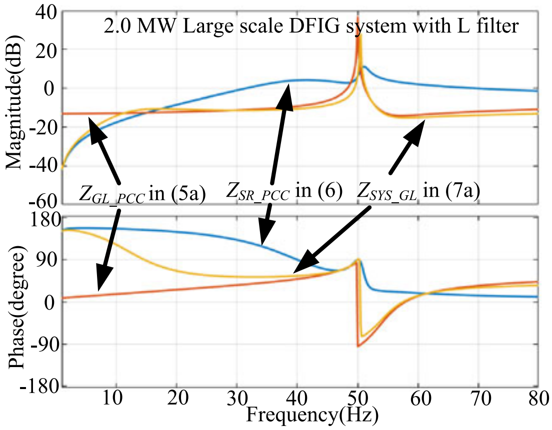

Fig. 12. Bode diagrams of large-scale DFIG system with *L* filter in the low-frequency range.

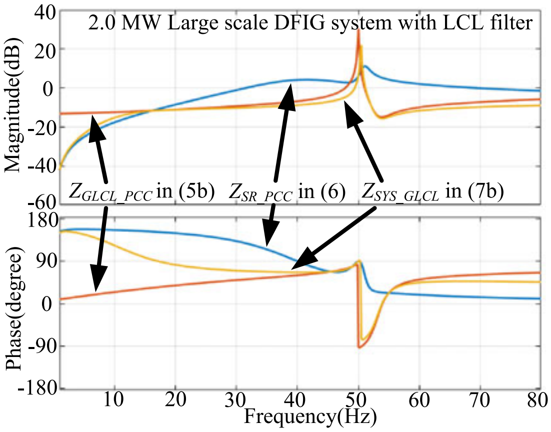

Fig. 13. Bode diagrams of large-scale DFIG system with *LCL* filter in the low-frequency range.

TABLE III
PARAMETERS OF PARALLEL COMPENSATED WEAK NETWORKS FOR SMALL- AND LARGE-SCALE DFIG SYSTEMS

For Small-Scale DFIG System			
R_{NETP}	0.1 Ω	L_{NETP}	1.5 mH
C_{NETP}	10 μF		
V_{PCC}	380 V	V_{HV}	380 V
K_3	1		
For Large-Scale DFIG System			
R_{NETP}	10.3 Ω	L_{NETP}	36.6 mH
C_{NETP}	1.02 μF		
V_{PCC}	1 kV	V_{HV}	25 kV
K_3	25		

TABLE IV
PARAMETERS OF SERIES COMPENSATED WEAK NETWORKS FOR SMALL- AND LARGE-SCALE DFIG SYSTEMS

For Small-Scale DFIG System			
R_{NETS}	1 mΩ	L_{NETS}	0.01 mH
C_{NETS}	0.1 F		
V_{PCC}	380 V	V_{HV}	380 V
K_3	1		
For Large-Scale DFIG System			
R_{NETS}	0.3 Ω	L_{NETS}	3.93 mH
C_{NETS}	520 μF		
V_{PCC}	1 kV	V_{HV}	25 kV
K_3	25		

It can be found that even if different L and LCL filters are adopted in Figs. 10 and 11, the impedances of the grid part $Z_{\mathrm{GL\_PCC}}$ and $Z_{\mathrm{GLCL\_PCC}}$ with different filters remain almost the same since these two impedances are dominated by the filter inductor L_f in the low-frequency range. As a result, the impedance shape of the DFIG system $Z_{\mathrm{SYS\_GL}}$ and $Z_{\mathrm{SYS\_}GLCL}$ are the same in the low-frequency range. Similar conclusions can be obtained in the case of the large-scale DFIG using L and LCL filters, as shown in Figs. 12 and 13.

B. Impedance Shape of the Weak Networks

According to [31]–[34], a wind farm is always connected through high-voltage long-distance transmission cables, which can be considered as series RL elements, together with either series or parallel compensated capacitance. Their impedance expressions are given in (9).

Table III shows the parameters of the parallel compensated weak networks for small- and large-scale DFIG systems, while the parameters of the series compensated weak networks for small- and large-scale DFIG systems are shown in Table IV.

It is important to clarify that in the parallel compensated weak network for the large-scale DFIG system in Table III, the voltage changing ratio $K_3 = 25$ needs to be considered in its impedance modeling, and thus, the actual parameter values of the parallel compensated weak network seen from the PCC in Fig. 1 can be calculated as $R_{\mathrm{NETP}}/K_3^2 = 16\,\mathrm{m}\Omega$, $L_{\mathrm{NETP}}/K_3^2 = 0.058\,\mathrm{mH}$, and $C_{\mathrm{NETP}} * K_3^2 = 637\,\mu\mathrm{F}$. Moreover, it needs to be pointed out that the large parallel network inductance $L_{\mathrm{NETP}} = 36.6\,\mathrm{mH}$ is possible due to the inductance of the long-distance transmission cables.

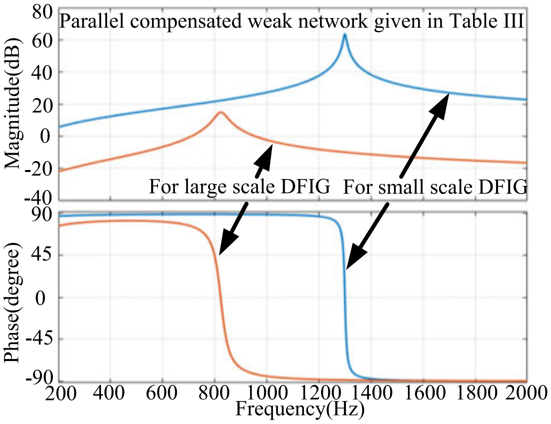

Fig. 14. Bode diagrams of the parallel compensated weak network for both small- and large-scale DFIG systems.

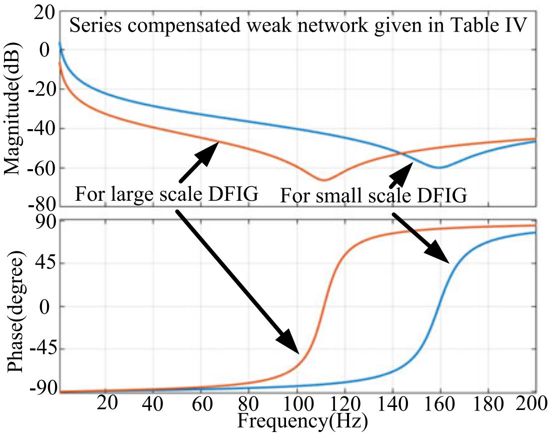

Fig. 15. Bode diagrams of the series compensated weak network for both small- and large-scale DFIG systems.

Similarly, in the series compensated weak network for the large-scale DFIG system given in Table IV, the voltage changing ratio $K_3 = 25$ also needs to be considered. As a result, the actual values of the series compensated weak network seen from the PCC, as shown in Fig. 1, can be calculated as $R_{\mathrm{NETS}}/K_3^2 = 0.48\,\mathrm{m}\Omega$, $L_{\mathrm{NETS}}/K_3^2 = 0.0063\,\mathrm{mH}$, and $C_{\mathrm{NETS}}{*}K_3^2 = 0.325\,\mathrm{F}$.

Based on (9), the Bode diagrams of the parallel and series compensated weak networks for both small- and large-scale DFIG systems are shown in Figs. 14 and 15.

According to Fig. 14, it can be seen that the parallel compensated weak network behaves inductive in the range lower than the peak frequency, while it behaves capacitive in the range higher than the peak frequency. This character determines that the HFR is only likely to happen at the capacitive high-frequency range, when the phase difference of 180° between the DFIG system and the parallel compensated weak network is likely to occur.

On the contrary, as shown in Fig. 15, the series compensated weak network behaves capacitive/inductive in the frequency range lower/higher than the peak frequency. As a result, the SSR

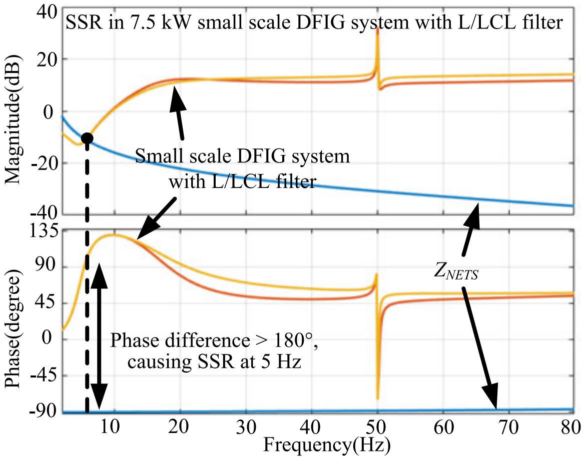

Fig. 16. SSR between small-scale DFIG system and series compensated weak network.

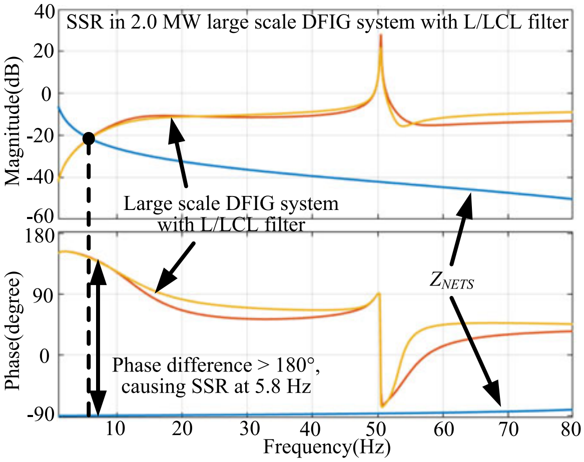

Fig. 17. SSR between large-scale DFIG system and series compensated weak network.

is only likely to occur at the low frequency, which is typically lower than the fundamental frequency.

C. Occurrence of SSR and HFR in the DFIG System

It is obvious that if the inductive unit and capacitive unit have equal magnitude, then the overall circuit impedance magnitude achieves a minimum value and a circuit resonance may occur.

Since the DFIG system remains inductive in most frequency range, as shown in Figs. 6–9, the weak network should behave capacitive in order to allow the resonance to happen. Both the SSR and HFR occur under the circumstance of the DFIG system behaving inductive and the weak network behaving capacitive, as shown in Figs. 16–19.

Fig. 16 shows the SSR between the small-scale DFIG system and the series compensated weak network, where the parameters used to plot this diagram are given in Tables I and IV. As it can be seen, only one magnitude intersection point exists at 5 Hz, and the phase difference is larger than 180°, which indicates the occurrence of SSR due to the negative resistance part in the DFIG system caused by the DFIG phase response of

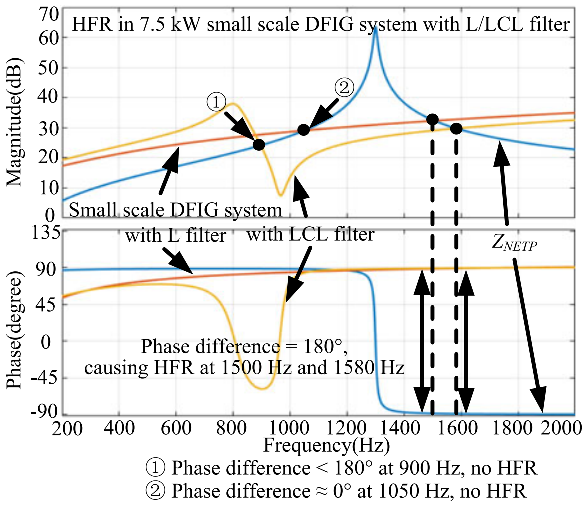

Fig. 18. HFR between small-scale DFIG system and parallel compensated weak network.

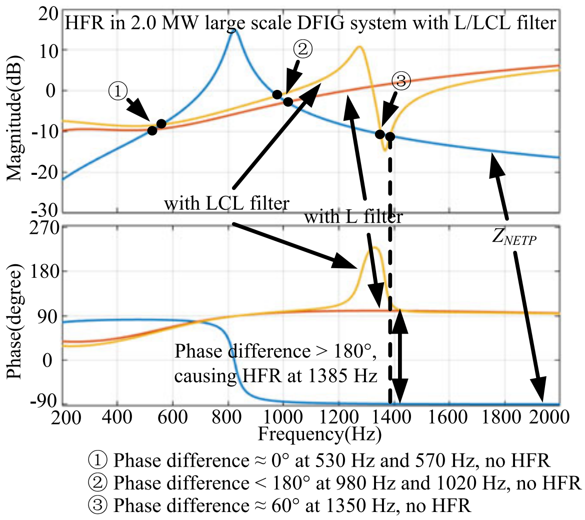

Fig. 19. HFR between large-scale DFIG system and parallel compensated weak network.

around 100°. Note that since the DFIG system with L or LCL filter has almost the same impedance response in the frequency range below 50 Hz, the SSR frequency is the same regardless of different L or LCL filter.

Similarly, Fig. 17 shows the SSR between the large-scale DFIG system and the series compensated weak network, and their parameters are available in Tables II and IV. The SSR frequency of 5.8 Hz occurs under this circumstance as a consequence of the phase difference larger than 180°.

In respect to the HFR in the small-scale DFIG system, it can be found from Fig. 18 that when a small-scale DFIG system with L or LCL filter is applied, the magnitude intersection points exist at 1500 and 1580 Hz, respectively, for the case of L filter and LCL filter. The phase difference of 180° at these intersection frequencies result in the occurrence of HFR. Nevertheless, it should be pointed out that there exists also other magnitude intersection points at 900 and 1050 Hz, but the resonances will not happen since the phase differences are smaller than 180°. The parameters to plot this diagram are available in Tables I and III.

Similarly, Fig. 19 shows the HFR between the large-scale DFIG system and the parallel compensated weak network. The large-scale DFIG system with LCL filter causes the HFR only at 1385 Hz due to the phase difference >180°. The magnitude intersection points at 570, 980, and 1350 Hz do not result in HFR as the phase difference < 180°. For the large-scale DFIG system with L filter, there are two magnitude intersection points at 530 and 1020 Hz, but the phase differences are smaller than 180° and helps to avoid the occurrence of HFR.

Therefore, based on aforementioned Bode diagrams in Figs. 16–19 and theoretical explanations, it can be concluded that both SSR and HFR are produced by following the same principle, i.e., the phase difference is equal to or larger than 180° at the magnitude intersection points, which result in the DFIG system inductive impedance part and the weak network capacitive impedance part to cancel out each other; then the overall impedance magnitude reaches its minimum value (or even negative value) and produce the SSR and HFR consequently.

D. HFR in Wind Farm With the Aggregated DFIG System

In the earlier analysis of the SSR and HFR, only one single DFIG system is investigated in order to conduct a detailed and specific investigation on the causes for SSR and HFR.

In practical applications, a wind farm with numbers of DFIG systems working together in parallel is a common type of wind power generation configuration. Therefore, it is important to discuss the HFR from the perspective of a large-scale wind farm.

Before investigating the HFR at the wind farm scale, it is important to evaluate the short-circuit ratio (SCR) of the discussed single DFIG system and its corresponding parallel compensated weak network listed in Tables II and III. It can be calculated that the HFR in single DFIG system is studied based on the condition of SCR = 20, as shown in the following equation:

$$\begin{aligned}\mathrm{SCR}_{\mathrm{HFR}} &= \frac{V_{\mathrm{HV}}^2}{(R_{\mathrm{NET}} + sL_{\mathrm{NET}})}\frac{1}{S_{\mathrm{DFIG}}}\\ &= \frac{3*(25\,kV/1.732)^2}{|10.3\,\Omega + j314*36.6\,\mathrm{mH}|}\frac{1}{2\mathrm{MW}} = 20\end{aligned} \tag{10}$$

where $V_{\mathrm{HV}} = 25$ kV, $R_{\mathrm{NETP}} = 10.3\ \Omega$, $L_{\mathrm{NETP}} = 36.6$ mH, the rated power of a single DFIG system is 2.0 MW; all these parameters are listed in Tables II and III.

It should be noted that the shunt capacitance is not included because it needs to be short-circuited when calculating the SCR in the case of the parallel compensated weak network in (10). Thus, without including the shunt capacitance C_{NET}, the SCR is assumed to be not quite appropriate to evaluate the weakness of the parallel compensated weak network, instead the SCR is just taken here to better compare the HFR discussed in single DFIG or wind farms in the following part.

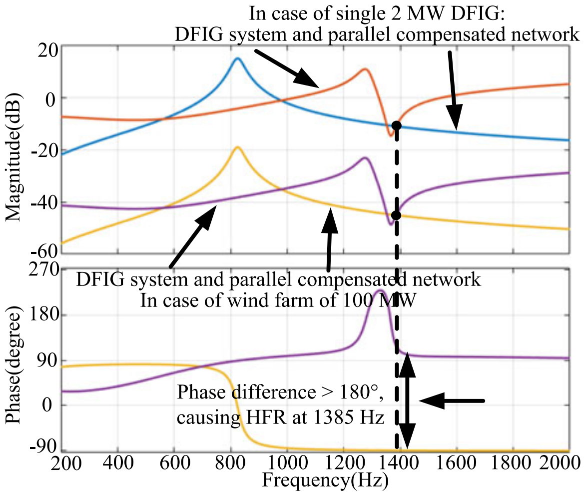

Fig. 20. HFR discussed in single 2.0 MW DFIG system or wind farm with 50 DFIG systems of 100 MW.

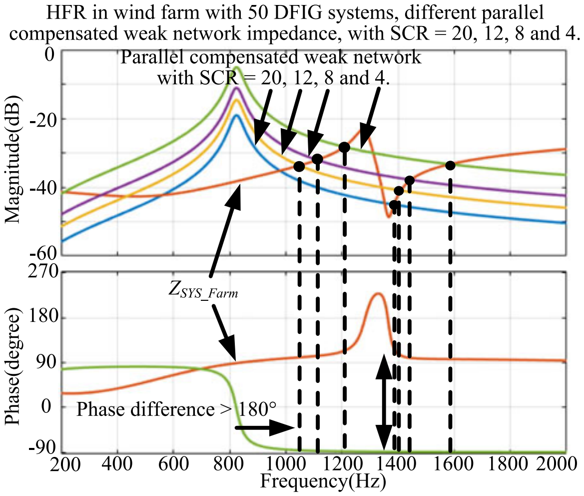

Fig. 21. HFR in wind farm with 50 DFIG systems, but different parallel compensated weak network impedance, with SCR = 20, 12, 8, and 4.

In order to study the HFR in the wind farm scale, the SCR is kept constant as the case of single DFIG. Considering the fact that in a typical wind farm, the DFIG systems are working in parallel connection; thus, the overall aggregated DFIG system parameters $Z_{\mathrm{SYS\_Farm}}$ can be derived by dividing the single DFIG system parameters using the number of included DFIG systems *n* in the wind farm [31]–[43]

$$Z_{\mathrm{SYS\_Farm}} = \frac{1}{n} Z_{\mathrm{SYS}} \tag{11}$$

where $Z_{\mathrm{SYS\_Farm}}$ is the impedance of the overall aggregated DFIG wind farm, Z_{SYS} is the impedance of single DFIG given in (7), and *n* is the number of DFIG systems included in the wind farm. In this discussion, *n* is chosen to be 50, where 50 DFIG systems are working in parallel in the wind farm and the overall aggregated rated power of the DFIG wind farm is 100 MW.

Moreover, according to (10) and 9(c), in order to keep the value of SCR in the wind farm the same as in the single DFIG system, the parameters of the parallel compensated weak network also needs to be divided by *n* as given in the following expression:

$$Z_{\mathrm{NETP\_Farm}} = \frac{1}{n} \frac{\left(sL_{\mathrm{NETP}}/K_3^2 + R_{\mathrm{NETP}}/K_3^2\right) \frac{1}{sK_3^2 C_{\mathrm{NETP}}}}{sL_{\mathrm{NETP}}/K_3^2 + R_{\mathrm{NETP}}/K_3^2 + \frac{1}{sK_3^2 C_{\mathrm{NETP}}}}. \tag{12}$$

Based on (11) and (12), the HFR at the wind farm scale, with 50 2.0 MW DFIG system working in parallel, can be investigated based on the Bode diagram shown in Fig. 20. Clearly, the impedance shapes of the single 2.0 MW DFIG system and the wind farm of 100 MW are the same, i.e., they have the same phase response, while the magnitude response becomes proportionally smaller. The same results can also be obtained in respect to the impedance shape of the parallel compensated weak network. Consequently, the HFR discussed in the single DFIG system and wind farm has the same result, i.e., the HFR at 1385 Hz will occur due to the phase difference is larger than 180°.

Furthermore, based on the discussions according to Fig. 20, the variation of the parallel compensated weak network impedance in the case of a wind farm is also discussed. The weak network impedance is divided by 50 (then the SCR is 20), 30 (then the SCR is 12), 20 (then the SCR is 8), and 10 (then the SCR is 4), and their Bode diagrams are shown in Fig. 21. As it is shown, when the SCR becomes smaller, i.e., the impedance of the parallel compensated weak network becomes larger and the networks becomes "weaker," the HFR will always occur and the resonance frequency becomes higher.

Thus, the following can be concluded: 1) the Bode diagram-based resonance analysis can be adopted to analyze the resonance in the case of both a single DFIG system as well as the wind farm with numbers of DFIG systems working in parallel; 2) the impedance of the aggregated DFIG system can be obtained by dividing the single DFIG system impedance with the numbers of DFIG systems [31]–[43]; and 3) as the parallel compensated weak network becomes weaker with larger impedance, the HFR always occurs at higher resonance frequencies.

Therefore, based on the discussion of HFR in single DFIG system in Figs. 18 and 19, HFR in the wind farm in Figs. 20 and 21, SSR in single DFIG system in Figs. 16 and 17, and SSR in a wind farm in [31]–[43], it can be found out that the proposed Bode diagram-based analysis method is effective and appropriate in respect to the HFR and SSR analysis.

IV. INFLUENCE FACTORS OF HFR AND SSR

As analyzed previously, the resonance frequencies of SSR and HFR are subject to several factors, including the following: 1) transformer configuration; 2) power scale of the DFIG system having different parameters; 3) *L* or *LCL* filter adopted in the GSC; 4) rotor speed; 5) closed-loop current controller parameters; and 6) the digital control delay.

Among these factors, the transformer configuration, rotor speed, and current closed-loop control proportional and integral parameters are possible to change in practical applications for a specific DFIG system. For instance, the voltage level is different and the transformer configuration may vary in many countries; the DFIG machine speed is subject to the wind speed variation and varies all the time; and the current control parameters need to be adjusted in practical situation in order to achieve an accurate and fast regulation of the output power.

Besides, the switching frequency $f_{\rm sw}$ and sampling frequency f_s of the large-scale DFIG system is lower than the small-scale system, i.e., $f_s = 10$ kHz and $f_{\rm sw} = 5$ kHz in a 7.5 kW small-scale DFIG system, and $f_s = 5$ kHz and $f_{\rm sw} = 2.5$ kHz in a 2.0 MW large-scale DFIG system. As a consequence, the digital control delay T_d, which is typically one and half sampling period, is also longer in the large-scale DFIG system, i.e., $T_d = 150$ μs in 7.5 kW DFIG system, and $T_d = 300$ μs in 2.0 MW DFIG system, as shown in Tables I and II. Nevertheless, the digital control delay remains constant for a certain DFIG system and will not vary in practical operation; thus, the digital control delay will not be investigated further here.

Based on the aforementioned discussion, only the influences of the following will be discussed further: 1) the transformer configuration; 2) the rotor speed; and 3) closed-loop current controller parameters.

A. *Influence of the Transformer Configuration*

As shown in Fig. 1, a three-terminal transformer is used to adjust the voltage level within the DFIG system, while a two-terminal step-up transformer is adopted to connect the low voltage side of the DFIG system to the high voltage side of the transmission cable. The voltage ratio of these two transformers may vary worldwide due to different voltage levels in different countries.

In order better to investigate the influence of the transformer turn ratio configuration, the large-scale 2.0 MW DFIG system with *LCL* filter is taken as an example, while the discussion of small-scale 7.5 kW DFIG system is neglected due to limited space in this paper.

Besides the network parameters in Tables III and IV, which are considered as group 1, it is assumed here that both the grid filter output voltage V_G, DFIG machine stator voltage $V_{\rm SR}$, and the PCC voltage $V_{\rm PCC}$ are all 690 V, while the transmission cable high voltage is 161 kV [31]–[34], [36], [37] as group 2. It should be noted that in practical applications, the voltage level increase is achieved by two step-up transformers in series connection to increase the voltage step by step. However, since it is assumed that the distance between these transformers is short, so during the impedance modeling process, these step-up transformers can be modeled as one single transformer with a high turns ratio. As a consequence, the $K_1 = K_2 = 1, K_3 = 161\,{\rm kV}/690\,{\rm V} = 233$, which is considered as group 2.

Figs. 22 and 23 show the Bode diagrams of the large-scale DFIG system impedance with two different transformer configurations. The SSR and HFR are discussed in Figs. 22 and 23, respectively. Due to the two different groups of transformer voltage turns ratios, the impedance shape of the large-scale DFIG system has slight changes. On the other hand, both the series and parallel compensated weak network also change as well and a much larger decrease in the magnitude response can be observed due to the large increase of K_3.

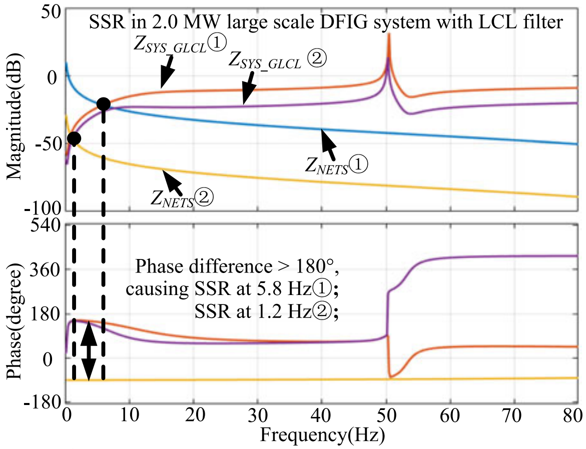

① $K_1 = 1000$ V/480 V, $K_2 = 1000$ V/690 V in Table II;
$K_3 = 25$ kV/1000 V in Table IV;
② $K_1 = 690$ V/690 V, $K_2 = 690$ V/690 V;
$K_3 = 161$ kV/690 V; assumed for discussion here only

Fig. 22. SSR between the large-scale DFIG system and the series compensated weak network when the transformer configuration changes.

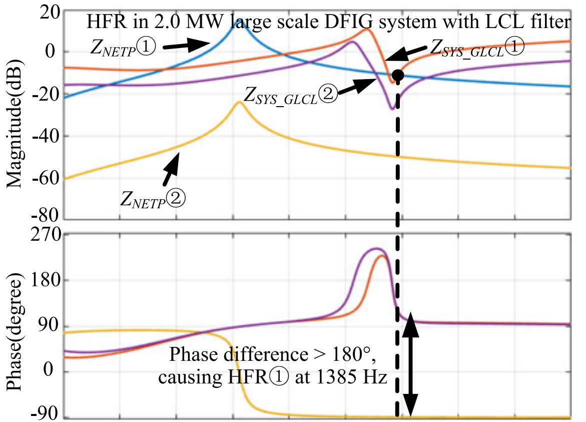

① $K_1 = 1000$ V/480 V, $K_2 = 1000$ V/690 V in Table II;
$K_3 = 25$ kV/1000 V in Table IV;
② $K_1 = 690$ V/690 V, $K_2 = 690$ V/690 V;
$K_3 = 161$ kV/690 V; assumed for discussion here only

Fig. 23. HFR between the large-scale DFIG system and the parallel compensated weak network when the transformer configuration changes.

It can be observed from Fig. 22 that, with the voltage turns ratio group 1, the SSR occurs at 5.8 Hz due to a phase difference >180° at the magnitude intersection point. However, once the transformer configuration changes to group 2, the magnitude intersection point shifts and the SSR frequency changes to 1.2 Hz, as a result. On the other hand, as it can be observed from Fig. 23 that the HFR at 1385 Hz occurs when the transformer configuration with parameters group 1 is applied; once the transformer configuration changes to parameter group 2, the magnitude intersection point no longer exists and the HFR will not happen.

Thus, it can be found that the transformer configuration is important to the impedance shape of the DFIG system and the weak network, consequently the occurrence of SSR and HFR as well as the resonance frequency is partly influenced by the transformer configuration.

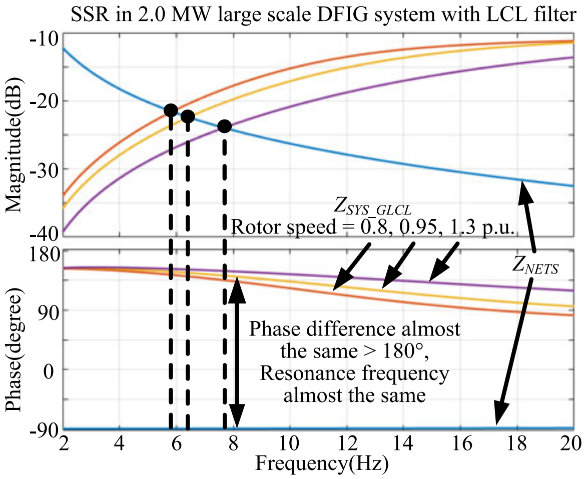

Fig. 24. SSR between the large-scale DFIG and the series compensated weak network at the rotor speed of 0.8, 0.95, and 1.3 p.u.

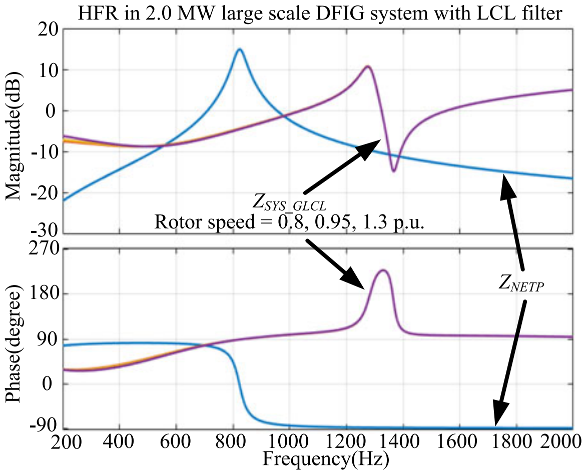

Fig. 25. HFR between the large-scale DFIG and the parallel compensated weak network at the rotor speed of 0.8, 0.95, and 1.3 p.u.

B. Influence of the Rotor Speed

According to the DFIG operation character, the DFIG system is able to deliver wind power within the rotor speed range of ±30%; thus, it is meaningful to investigate the influence of rotor speed on the SSR and HFR.

Figs. 24 and 25 show the Bode diagram of the large-scale DFIG system impedance at the rotor speeds of 0.8, 0.95, and 1.3 p.u., with the SSR and HFR considered.

As it can be seen from Fig. 24 regarding the SSR, the magnitude response of the large-scale DFIG system in the low-frequency range has obvious changes at different rotor speeds of 0.8, 0.95, and 1.3 p.u., which results in the magnitude intersection points to shift from 6 to 8 Hz, and most importantly, the magnitude response at the intersection points drops from -21 to -24 dB. Besides, the phase response of the large-scale DFIG system at the intersection points remains almost the same around 140° under all three different rotor speeds.

Based on the earlier description, it can be found that for the three cases with different rotor speeds, the impedance of the large-scale DFIG system can always be considered as a combination of negative resistance and positive inductance due to the same phase response of 140°; nevertheless, its magnitude decreases as the rotor speed increases. This means the amplitude of the negative resistance in the large-scale DFIG system becomes smaller, which is helpful to the DFIG system operation stability, and as a result, the SSR is less likely to happen when the rotor speed is higher.

On the other hand, based on the analysis in Fig. 25, it can be found that the impedance of the large-scale DFIG system at the potential HFR range remains the same regardless of the rotor speed variation, and exactly the same magnitude and phase response can be ensured. Therefore, it can be concluded that the rotor speed is not important to the HFR of the large-scale DFIG system.

C. Influence of the Current Controller Parameters

The current closed-loop control in the RSC and GSC may need to adjust their parameters $K_{\mathrm{prsc}}, K_{\mathrm{irsc}}, K_{\mathrm{pgsc}}$, and K_{igsc} for accurate and fast regulation of the DFIG output power. Thus, it is meaningful to discuss the influence of these parameters on the DFIG system impedance.

Three different groups of parameters are discussed in this section, i.e., group 1: $K_{\mathrm{prsc}} = 0.2$ and $K_{\mathrm{pgsc}} = 0.05$; group 2: $K_{\mathrm{prsc}} = 0.1$ and $K_{\mathrm{pgsc}} = 0.025$; and group 3: $K_{\mathrm{prsc}} = 0.04$ and $K_{\mathrm{pgsc}} = 0.01$.

Before discussing the influence of the current controller parameters on the SSR and HFR, the control bandwidth of current control with the three groups of parameters need to be demonstrated. In order to investigate the control bandwidth, the transfer function of the rotor current closed-loop control in the RSC can be presented as (Note that the rotor current control is taken as an example, while the grid side current control in GSC is neglected for simplicity.)

$$G_{cl}(s) = \frac{G_c(s)G_d(s)G_p(s)}{1 + G_c(s)G_d(s)G_p(s)} \tag{13}$$

where $G_c(s)$ is the PI current controller in (1), $G_d(s)$ is the digital control delay in (14), $G_p(s)$ is the control subject DFIG transfer function defined as $G_p(s) = 1/(R_r + s\sigma L_r)$ in [16], R_r is the rotor resistance, $L_r = L_m + L_{\sigma r}$ is the rotor inductance, L_m is the mutual inductance, and $L_{\sigma r}$ is the rotor leakage inductance. $\sigma = 1 - L_m^2/L_r L_s$ is the leakage inductance coefficient.

Fig. 26 shows the Bode diagram of the rotor current closed-loop control transfer function based on (13) with three different groups of parameters as mentioned earlier. It can be seen, when group 1 parameter $K_{\mathrm{prsc}} = 0.2$ is chosen, the rotor current closed-loop control bandwidth is 800 Hz, which is large enough to achieve fast dynamic response of the rotor current control. On the other hand, for the other two groups of parameters, the control bandwidth becomes much lower as 270 and 90 Hz. A similar conclusion considering the GSC current closed-loop control can be obtained and will not be described in detail here.

Figs. 27 and 28 show the SSR and HFR between the large-scale DFIG system and the weak network when the

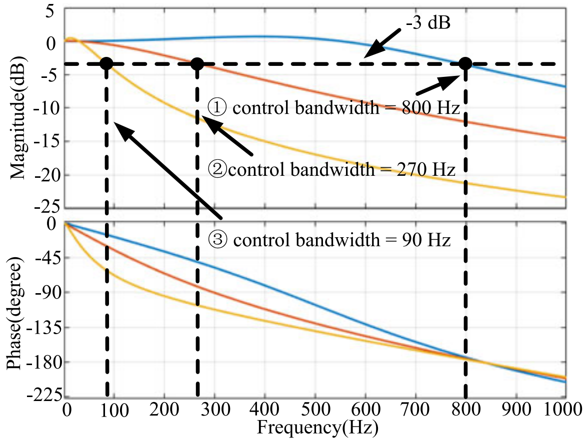

Fig. 26. Bode diagram of the rotor current closed-loop control transfer function in (13), with group 1: $K_{\mathrm{prsc}} = 0.2$; group 2: $K_{\mathrm{prsc}} = 0.1$; and group 3: $K_{\mathrm{prsc}} = 0.04$.

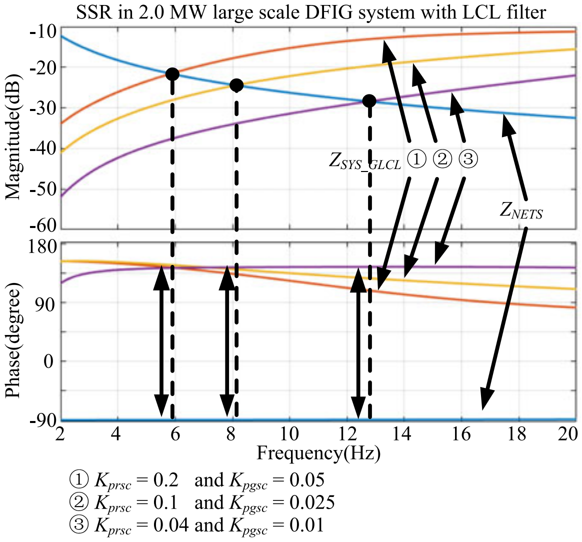

Fig. 27. SSR between large-scale DFIG and series compensated weak network when current closed control parameters in RSC and GSC change, group 1: $K_{\mathrm{prsc}} = 0.2$ and $K_{\mathrm{pgsc}} = 0.05$; group 2: $K_{\mathrm{prsc}} = 0.1$ and $K_{\mathrm{pgsc}} = 0.025$; and group 3: $K_{\mathrm{prsc}} = 0.04$ and $K_{\mathrm{pgsc}} = 0.01$.

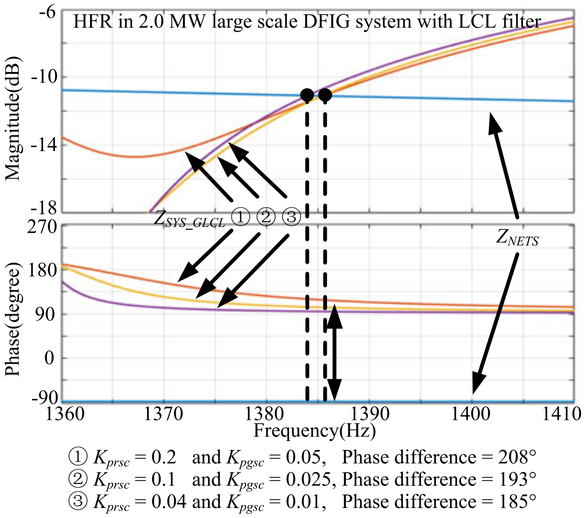

Fig. 28. HFR between large-scale DFIG and parallel compensated weak network when current closed control parameters in RSC and GSC change, group 1: $K_{\mathrm{prsc}} = 0.2$ and $K_{\mathrm{pgsc}} = 0.05$; group 2: $K_{\mathrm{prsc}} = 0.1$ and $K_{\mathrm{pgsc}} = 0.025$; and group 3: $K_{\mathrm{prsc}} = 0.04$ and $K_{\mathrm{pgsc}} = 0.01$.

closed-loop control parameters in the RSC and GSC change, group 1: $K_{\mathrm{prsc}} = 0.2$ and $K_{\mathrm{pgsc}} = 0.05$; group 2: $K_{\mathrm{prsc}} = 0.1$ and $K_{\mathrm{pgsc}} = 0.025$; and group 3: $K_{\mathrm{prsc}} = 0.04$ and $K_{\mathrm{pgsc}} = 0.01$. It should be noted that compared with the integral parameters K_{irsc} and K_{igsc}, the proportional parameters K_{prsc} and K_{pgsc} have dominant influence on the DFIG system impedance, and thus, only the variations of proportional parameters are discussed here.

According to Fig. 27, as the proportional parameters of the RSC and GSC decrease, the magnitude intersection frequency points shift from 6 to 8 Hz and 13 Hz, while the phase difference at these frequency points remain almost the same >180°. But it also needs to be pointed out that as the controller parameters become smaller, the amplitude of the negative resistance of DFIG system at the three intersection points becomes smaller, which is helpful to the DFIG system stability. Thus, it can be concluded that the SSR in the large-scale DFIG system is less likely to happen when smaller current control parameters with lower bandwidth is adopted.

The HFR with different current control parameters are shown in Fig. 28. When the proportional parameters of the RSC and GSC decrease, both the magnitude response and phase response of the large-scale DFIG system have minor changes and the magnitude intersection points have minor changes from 1385 to 1383 Hz, and the phase difference decreases from 208° to 193° and 185°, respectively. Thus, it can be found that, as the proportional parameters of the current closed-loop control in RSC and GSC change, the large-scale DFIG system HFR still exists due to a phase difference larger than 180°, and the HFR resonance frequency remains almost the same. Thus, the proportional parameters are not important to the large-scale DFIG system HFR frequency.

V. ACTIVE DAMPING STRATEGY FOR HFR

As mentioned in the previous sections, the resonances can be mitigated if the impedance shape of the DFIG system or the weak network can be appropriately modified.

Modifying the impedance of the weak network is an effective method to mitigate the resonance. For instance, thyristor-controlled series capacitors [32] and gate-controlled series capacitors [33] are demonstrated, respectively, to reshape the network impedance, thus avoiding the potential SSR.

However, not only the DFIG-based wind power system but also the other renewable power generation sources and various types of loads are likely to be connected to the weak network. Therefore, if the impedance character of the weak network is modified, then potential operation problems may be produced for the other connected sources and loads. So in this paper, only the impedance reshaping in the DFIG system through the introduction of virtual impedance is investigated.

Note that only the mitigation of HFR through virtual impedance is discussed in this section. For the SSR, there are two reasons to make the virtual impedance-based active damping strategy inappropriate for the SSR damping:

1) The SSR frequency is likely to be close to the fundamental components of the stator and rotor voltage and currents; thus, the introduction of the virtual impedance at the potential SSR frequency may affect the normal control of the rotor and stator current fundamental components and cause problems of wind power generation as a consequence.
2) As discussed in Fig. 27 and [31], the parameters of the PI controller have obvious influence on the DFIG system impedance shape at the low-frequency range (<50 Hz). Therefore, in order to appropriately reshape the DFIG system impedance to mitigate the SSR, the parameters of the virtual impedance need to be carefully designed and adjusted when different current control parameters are applied, thus making the active damping strategy complicated and less applicable in practice.

Since the machine part and the grid part of the DFIG system are in parallel connection, the impedance reshaping in either the machine part or the grid part can be adopted. For the machine part reshaping, both the rotor part and the stator part can be used to implement the impedance modification. Therefore, in the following discussions, the introduction of the virtual impedance in three ways is discussed, i.e., in the grid part, in the rotor part and in the stator part of the DFIG system.

A. Introduction of Virtual Impedance

The virtual impedance needs to be introduced in order to achieve the appropriate DFIG system impedance reshaping. Since the phase difference$>=180°$ between the DFIG system and the parallel compensated weak network at the magnitude intersection frequency point is the direct reason of the HFR, reducing the phase difference can help to mitigate the resonance. Due to the inductive behavior of the DFIG system with phase response larger than 90° in the potential HFR range, the insertion of a capacitive unit can be helpful in order to reduce its phase response.

However, the digital control delay is inevitable in the DFIG system as discussed in (14), and as a consequence, the originally introduced virtual positive resistance (PR) can be transformed into the combination of positive resistance and positive capacitance (PC), as illustrated in Fig. 29

$$G_d(s) = e^{-sT_d} \tag{14}$$

where $T_d = 150\ \mu$s is the control delay and $T_s = 100\ \mu$s is the sampling period in the small-scale DFIG system, as shown in Table I.

According to Fig. 29, the digital control delay $T_d = 150\ \mu$s causes a phase angle delay $\Delta\theta$, which can be calculated based on (14) as

$$\Delta\theta = -2\pi f T_d. \tag{15}$$

Based on (15), it can be found that the phase angle delay $\Delta\theta$ varies from $-54°$ at 1000 Hz to $-108°$ at 2000 Hz. This means that the phase angle delay $\Delta\theta$ is helpful by producing the PC [see Fig. 29(b)] and the DFIG system phase response can be reduced.

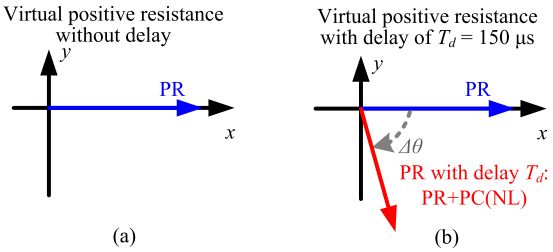

Fig. 29. Vector diagram of the virtual positive resistance without/with digital control delay $T_d = 150\ \mu s$; PR, positive resistance; PC, positive capacitance; NL, negative inductance.

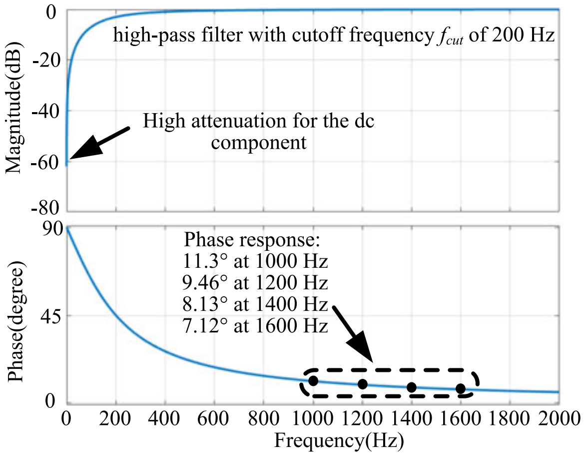

Fig. 30. Bode diagram of the high-pass filter with the cutoff frequency $f_{\text{cut}} =$ 200 Hz.

Nevertheless, the virtual impedance will influence the entire frequency range, and the rotor current fundamental component control may be affected unfavorably. Thus, a high-pass filter needs to be introduced in order to avoid the influence of the virtual impedance in the low-frequency range

$$G_{\text{hp}}(s) = \frac{s}{s + 2\pi f_{\text{cut}}} \tag{16}$$

where f_{cut} is the cutoff frequency of the high-pass filter.

Fig. 30 shows the Bode diagram of the high-pass filter, with a cutoff frequency $f_{\text{cut}} = 200$ Hz. Clearly, a high-pass filter is able to produce zero gain for the dc component. Thus, the influence of the virtual positive resistance on the error dc component can be eliminated.

Besides, the high-pass filter has a leading phase response, which can be calculated based on (16) as

$$\angle G_{\text{hp}}(j\omega) = \arctan\left(\omega_{\text{cut}}/\omega\right). \tag{17}$$

The phase-leading results can be seen from Fig. 30, i.e., 11.3° at 1000 Hz, 9.46° at 1200 Hz, 8.13° at 1400 Hz, and 7.12° at 1600 Hz.

Then, the virtual impedance Z_v, including the virtual positive resistance R_v, the high-pass filter in (16), as well as the digital

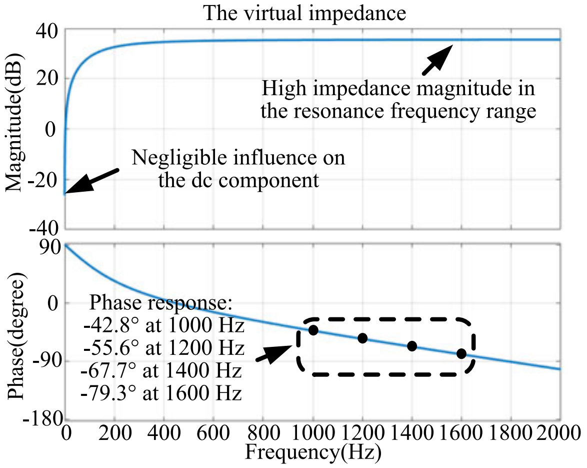

Fig. 31. Bode diagram of the virtual impedance including the virtual positive resistance $R_v = 60\,\Omega$ and the high-pass filter cutoff frequency $f_{\mathrm{cut}} = 200$ Hz, with control delay of $T_d = 150\,\mu$s.

control delay in (14), can be presented as

$$Z_v(s) = R_v \frac{s}{s + 2\pi f_{\mathrm{cut}}} e^{-sT_d}. \tag{18}$$

Fig. 31 shows the Bode diagram of the virtual impedance, including the virtual positive resistance $R_v = 60\,\Omega$ and the high-pass filter cutoff frequency $f_{\mathrm{cut}} = 200$ Hz, with a control delay of $T_d = 150\,\mu$s. As it can be seen, due to the use of the high-pass filter, the influence on the dc component is eliminated, while a high impedance magnitude in the potential HFR range can be obtained, which helps to damp the HFR. Besides, the phase responses are $-42.8°$ at 1000 Hz, $-55.6°$ at 1200 Hz, $-67.7°$ at 1400 Hz, and $-79.3°$ at 1600 Hz. This phase response means that the virtual impedance behaves as a combination of the positive resistance (helpful to increase the DFIG system resistance) and the PC (helpful to reduce the DFIG system phase response).

B. Impedance Reshaping Through DFIG Grid Part

Since the branch of the GSC and L_f is in a parallel connection with the C_f branch, thus according to the parallel impedance equation, the virtual impedance will play a more significant role of the impedance reshaping, if it is inserted in series with the grid side filter L_g. Fig. 32 shows the grid part with the virtual impedance in the grid part.

Based on Fig. 32, the DFIG system impedance with the reshaped grid side impedance can be presented as (19b) shown at the bottom of the page.

$$Z_{\mathrm{SYS\_Gv}} = \frac{Z_{\mathrm{Gv}} Z_{\mathrm{SR}}}{Z_{\mathrm{Gv}} + Z_{\mathrm{SR}}} \tag{19a}$$

Fig. 33 shows the Bode diagram of the DFIG system impedance with the virtual impedance in the grid part, $R_v = 50\ \Omega$, $f_{\mathrm{cut}} =$ 1400 Hz, and $T_d = 150\ \mu$s. As shown in Fig. 33, before the virtual impedance is implemented, the original phase difference between the small-scale DFIG system Z_{SYSTEM} and the parallel compensated weak network Z_{NETP} is 180°, which causes the HFR; on the other hand, once the virtual impedance is employed, the phase difference can be reduced to 149°, thereby achieving the active damping successfully. Therefore, the effectiveness of reshaping DFIG system impedance with a virtual impedance in the grid part can be validated.

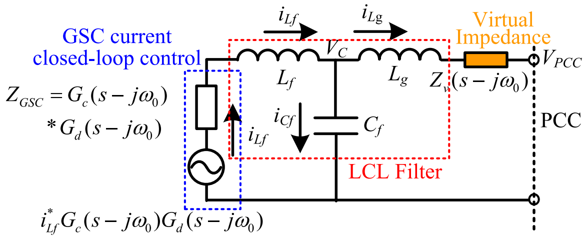

Fig. 32. Impedance modeling of the grid part (including GSC and *LCL* filter) with the virtual impedance.

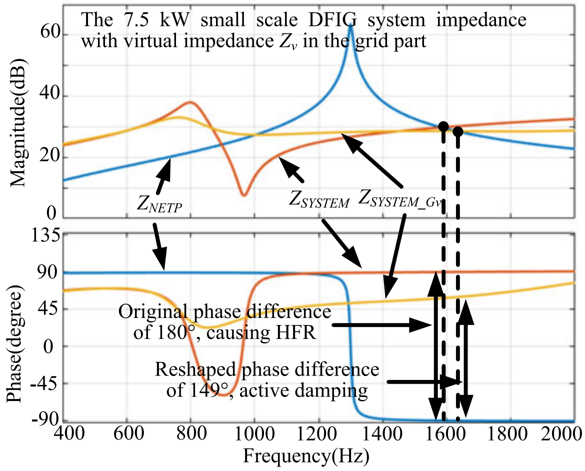

Fig. 33. Bode diagram of the small-scale DFIG system impedance with the virtual impedance in the grid part, $R_v = 50\ \Omega$, $f_{\mathrm{cut}} = 1400$ Hz, and $T_d = 150\ \mu$s.

In order to achieve an appropriate impedance reshaping, the parameters of virtual impedance in (18), i.e., the virtual resistance R_v and the high-pass filter cutoff frequency f_{cut}, need to be carefully designed.

The phase delay caused by the digital control delay is presented in (18), and the phase leading introduced by the high-pass filter is given in (17). Thus, based on these two equations, the phase response of the virtual impedance at the resonance frequency can be calculated as

$$\angle Z_{v\,|f=f_{\mathrm{reso}}} = \arctan\left(f_{\mathrm{cut}}/f_{\mathrm{reso}}\right) - 2\pi f_{\mathrm{reso}} T_d. \tag{20}$$

$$Z_{\mathrm{Gv}} = \frac{Z_{C_f}\left(Z_{L_f} + Z_{\mathrm{GSC}}\right) + \left(Z_{L_g} + Z_v\right)\left(Z_{L_f} + Z_{\mathrm{GSC}}\right) + Z_{C_f}\left(Z_{L_g} + Z_v\right)}{Z_{C_f} + \left(Z_{L_f} + Z_{\mathrm{GSC}}\right)}. \tag{19b}$$

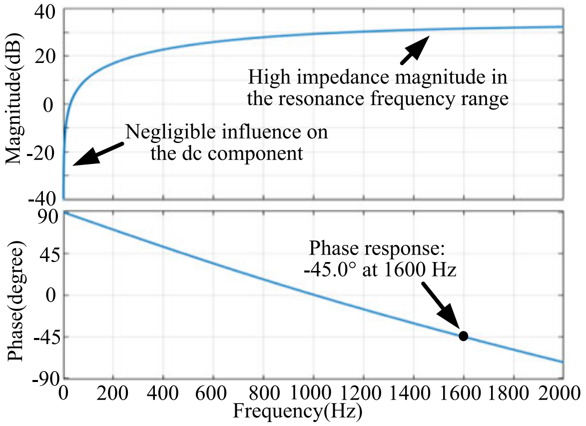

Fig. 34. Bode diagram of the virtual impedance, including the virtual positive resistance $R_v = 50\,\Omega$ and the high-pass filter cutoff frequency $f_{\mathrm{cut}} = 1400$ Hz, with control delay $T_d = 150\ \mu$s.

In order to appropriately reshape the impedance of the DFIG system, the phase response of the virtual impedance Z_v in (20) is preferred to be $\angle Z_{v\,|f=f_{\mathrm{reso}}} = -45°$. This phase response indicates that the virtual positive resistance and virtual PC have the same magnitude, and the PC is able to decrease the phase response of the DFIG system, while the positive resistance is able to improve the DFIG system rejection capability against the resonance.

Then, based on (20), the high-pass filter cutoff frequency can be obtained as

$$f_{\mathrm{cut}} = f_{\mathrm{reso}} \tan\left(\angle Z_{v\,|f=\,f_{\mathrm{reso}}} + 2\pi f_{\mathrm{reso}} T_d\right) \tag{21}$$

where f_{reso} is the resonance frequency, f_{cut} is the high-pass filter cutoff frequency in (16), T_d is the digital control delay in (14), and Z_v is the virtual impedance in (15).

It can be observed from (21) that the high-pass filter cutoff frequency f_{cut} is determined by several parameters, i.e., resonance frequency f_{reso}, digital control delay T_d, and expected virtual impedance phase response $\angle Z_{v\,|f=f_{\mathrm{reso}}}$.

By substituting $f_{\mathrm{reso}} = 1600$ Hz, $T_d = 150\ \mu$s and the expected phase response of $-45°$ into (21), the cutoff frequency can be calculated as $f_{\mathrm{cut}} = 1410$ Hz.

In order effectively to reduce the phase response of the DFIG system, the magnitude of the introduced virtual PC should be larger than the magnitude of the grid part impedance in the HFR range, as expressed in the following,

$$R_v \sin\left(\angle Z_{v\,|f=\,f_{\mathrm{reso}}}\right) > |Z_G| \tag{22}$$

where R_v is the virtual positive resistance in (18).

It can be observed that the virtual resistance is determined by the DFIG grid part impedance magnitude Z_G, as well as the expected phase response of the virtual impedance $\angle Z_{v\,|f=f_{\mathrm{reso}}}$. By substituting the small-scale DFIG system parameters in Table I, the virtual resistance can be calculated as $R_v > 43\ \Omega$.

Fig. 34 shows the Bode diagram of the virtual impedance with the parameters from the earlier design, i.e., $f_{\mathrm{cut}} = 1400$ Hz, $R_v = 50\ \Omega$. It can be observed that the phase response of the virtual impedance at the original HFR frequency 1600 Hz is $-45°$. This phase response indicates that the virtual impedance will behave as a combination of a virtual resistance and a virtual capacitance with the same magnitude, and both of them are helpful for the mitigation of HFR.

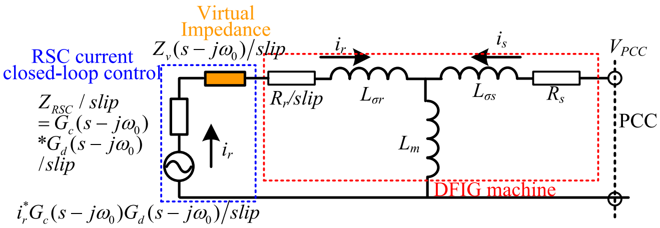

Fig. 35. Impedance modeling of the RSC and DFIG machine with the virtual impedance in the rotor part.

Thus, it can be seen that the earlier discussion gives out a design procedure of the virtual impedance parameters implemented in the grid part of the DFIG system, and the Bode diagram with the reshaped DFIG system impedance is plotted in Fig. 33 where the virtual impedance parameters are $f_{\mathrm{cut}} = 1400$ Hz and $R_v = 50\ \Omega$. The successful mitigation of HFR, as described in Fig. 33, is able to validate the parameter design results.

C. Impedance Reshaping Through DFIG Rotor Part

As discussed earlier, the virtual impedance can also be inserted in the rotor part of the DFIG system. Fig. 35 shows the impedance modeling of the RSC and DFIG machine with the virtual impedance in the rotor part.

Thus, the DFIG system impedance, including the virtual impedance in the rotor part, can be presented as

$$Z_{\mathrm{SYS}\_R_v} = \frac{Z_G Z_{\mathrm{SR}\_R_v}}{Z_G + Z_{\mathrm{SR}\_R_v}} \tag{23a}$$

$$Z_{\mathrm{SR}\_R_v} = \frac{Z_{L_m} H_{R_v} + (R_s + Z_{L_{\sigma s}}) H_{R_v} + Z_{L_m} (R_s + Z_{L_{\sigma s}})}{Z_{L_m} + H_{R_v}} \tag{23b}$$

where $H_{\mathrm{Rv}} = (R_r + Z_{\mathrm{RSC}} + Z_v)/\mathrm{slip}{+}Z_{L\sigma r}$.

Fig. 36 shows the Bode diagram of the DFIG system impedance with the virtual impedance in the rotor part, $R_v = 120\ \Omega$, $f_{\mathrm{cut}} = 1400$ Hz, and $T_d = 150\ \mu$s. As shown in Fig. 36, once the virtual impedance is implemented in the DFIG rotor part, the phase difference can be successfully reduced from 180° to 153° and the mitigation of the HFR can be achieved. Therefore, reshaping the DFIG system impedance using the virtual impedance in the rotor part can be verified.

The parameters of the virtual impedance inserted in the rotor part also need to be designed appropriately. Note that the high-pass filter cutoff frequency design is only determined by the resonance frequency f_{reso}, the digital control delay T_d, and the expected virtual impedance phase response $\angle Z_{v\,|f=f_{\mathrm{reso}}}$. Therefore, the design result of f_{cut} should be the same and will not be repeated here.

The magnitude of the virtual resistance R_v can be designed similarly as in the case in Section V-B, i.e., the magnitude of

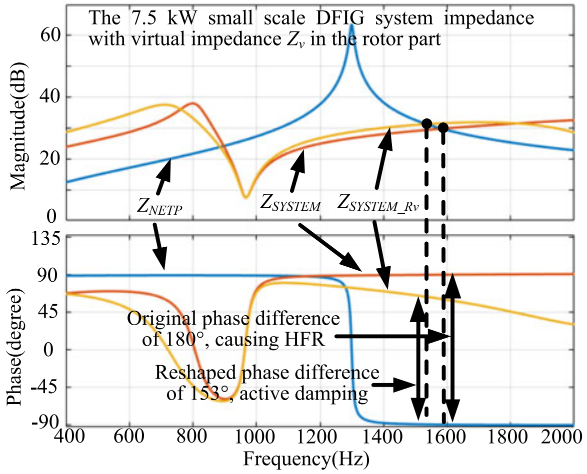

Fig. 36. Bode diagram of the small-scale DFIG system impedance with virtual impedance in the rotor part, $R_v = 120\ \Omega$, $f_{\rm cut} = 1400$ Hz, and $T_d = 150\ \mu$s.

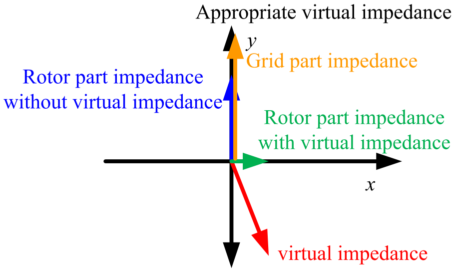

Fig. 37. Vector diagram of DFIG impedances applying an appropriate virtual impedance.

the virtual PC should be larger than the magnitude of $Z_{\rm SR}$ at the resonance frequency.

Considering the fact that the DFIG mutual inductance L_m is much larger than the stator and rotor leakage inductance $L_{\sigma s}$ and $L_{\sigma r}$, the mutual inductance branch can be neglected, and the simplified impedance of $Z_{\rm SR}$ at the HFR resonance frequency can be calculated as the sum of $L_{\sigma s}$ and $L_{\sigma r}$. Thus, the following equation can be deduced:

$$R_v \sin\left(\angle Z_{v|f=f_{\rm reso}}\right) > 2\pi f_{\rm reso}\left(L_{\sigma s} + L_{\sigma r}\right). \tag{24}$$

According to the small-scale DFIG system parameter in Table III, the virtual resistance inserted in the rotor part can be calculated as $R_v = 120\ \Omega$. The Bode diagram of the reshaped DFIG system impedance is shown in Fig. 36, which helps to validate the correctness of the parameter design result.

Furthermore, the design result of R_v in (24) only defines the minimum value, and it is necessary to discuss the DFIG system impedance reshaping result when too large R_v is adopted. Fig. 37 shows the vector diagram of the DFIG impedances with the appropriate virtual impedance, and Fig. 38 shows the vector diagram of DFIG impedances with too large virtual impedance.

As can be seen from Fig. 37, when an appropriate virtual impedance is applied (in red), the original “rotor part impedance without virtual impedance (in blue)” can be transformed to “the rotor part impedance with virtual impedance (in green),” and its phase response changes from 90° to 0°. Note that the magnitude

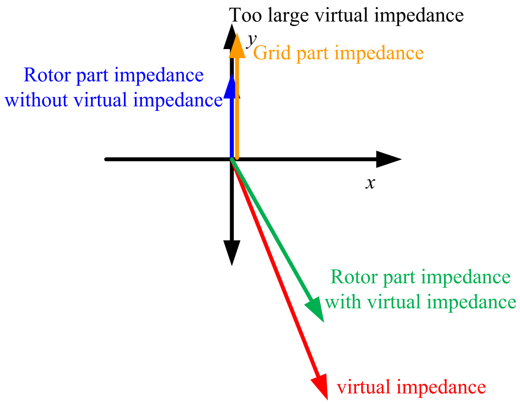

Fig. 38. Vector diagram of the DFIG impedances with a too large virtual impedance.

of “the rotor part impedance with virtual impedance (in green)” is much smaller than “the grid part impedance (in yellow).”

Considering the fact that the rotor part impedance and the grid part impedance are in parallel connection, the overall DFIG system impedance will mainly be determined by “the rotor part impedance with virtual impedance (in green)” due to its smaller magnitude, indicating the phase response of the DFIG system can be greatly reduced from the original 90°, thus sufficient phase margin can be achieved, as shown in Fig. 36, and the HFR can be mitigated.

Nevertheless, for the case of too large virtual impedance, as shown in Fig. 38, “the rotor part impedance with virtual impedance (in green)” has much larger magnitude than “the grid part impedance (in yellow)” due to the “too large virtual impedance (in red).”

Similarly, considering the fact that the rotor part impedance and the grid part impedance are in parallel connection, therefore the overall DFIG system impedance will mainly be determined by “the grid part impedance (in yellow)” due to its smaller magnitude and indicating the phase response of the DFIG system will almost remain 90°, thus the HFR still exists and the active damping fails.

In order to better validate the earlier vector diagram-based analysis, a Bode diagram of the DFIG system impedance with both appropriate and too large virtual impedance is plotted in Fig. 39. It can be seen, when the appropriate $R_v = 120\ \Omega$ is adopted, the active damping can be achieved with a phase difference $=$ 153°. On the other hand, when too large $R_v = 600\ \Omega$ is adopted, the active damping may fail due to a phase difference $=$ 176°. Furthermore, when even larger $R_v = 1200\ \Omega$ is adopted (which is not plotted, otherwise it is difficult to see clearly), the active damping will fail due to a phase difference $=$ 180°.

Therefore, based on earlier explanations, it can be found that when too large virtual impedance is applied, the DFIG system is instable because the overall impedance character of the DFIG system does not change significantly, as shown in Fig. 39, and the active damping may fail because the phase difference between the DFIG system and the parallel compensated weak network remains 180°.

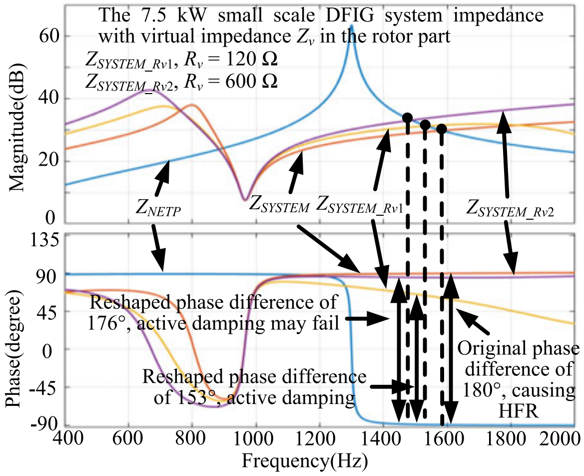

Fig. 39. Bode diagram of the small-scale DFIG system impedance with virtual impedance in the rotor part, $R_v = 120$ or $600\ \Omega$, $f_{\mathrm{cut}} = 1400$ Hz, and $T_d = 150\ \mu$s.

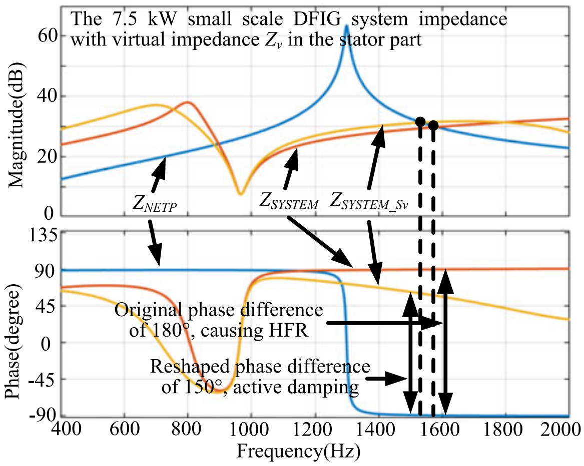

Fig. 41. Bode diagram of the small-scale DFIG system impedance with the virtual impedance in the stator part, $R_v = 120\ \Omega$, $f_{\mathrm{cut}} = 1400$ Hz, $T_d = 150\ \mu$s.

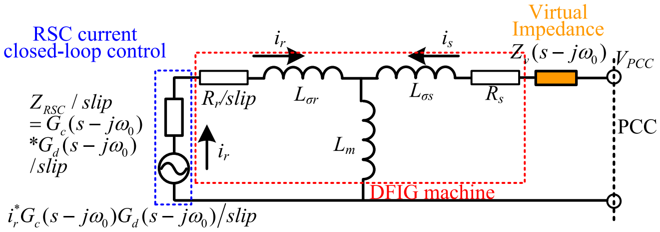

Fig. 40. Impedance modeling of the RSC and DFIG machine with the virtual impedance in the stator part.

A similar design result of the virtual impedance parameters regarding the implementation in the grid part and the stator part can be obtained; thus, it will not be described here for the sake of simplicity.

D. Impedance Reshaping Through the DFIG Stator Part

Besides the rotor part, the virtual impedance can also be inserted to the DFIG stator part, as shown in Fig. 40.

Thus, the DFIG system impedance including the virtual impedance in the stator part can be presented as

$$Z_{\mathrm{SYS}\_Sv} = \frac{Z_G Z_{SR\_Sv}}{Z_G + Z_{SR\_Sv}} \tag{25a}$$

$$Z_{SR\_Sv} = \frac{Z_{L_m} H + (R_s + Z_{L_{\sigma s}} + Z_v) H + Z_{L_m} (R_s + Z_{L_{\sigma s}} + Z_v)}{Z_{L_m} + H} \tag{25b}$$

where all the variables are defined in (6) and (18).

Fig. 41 shows the Bode diagram of the DFIG system impedance with the virtual impedance in the stator part, $R_v = 120\ \Omega$, $f_{\mathrm{cut}} = 1400$ Hz, $T_d = 150\ \mu$s. By comparing Figs. 39 and 41, it can be found that the reshaped DFIG system with the virtual impedances in the rotor part and the stator part are almost the same, i.e., the reshaped phase differences are 153° and 150°, respectively, in each case. This result can be explained as, since the DFIG mutual inductance L_m is comparatively much larger than the inductance of the rotor branch; thus, the mutual inductance can be reasonably neglected [31]. As a result, the rotor part and stator part of the DFIG system can be regarded as in series connection and the virtual impedance introduced either in the rotor part or the stator part will have almost the same impedance reshaping performance. Hence, the mitigation of HFR with virtual impedance in the stator part can be validated.

As for the virtual impedance parameters design in the stator part, it can be found that the design results are the same as in the case of the rotor part due to the series connection of the DFIG stator leakage inductance and the rotor leakage inductance. Thus, the parameter design will not be repeated.

VI. Simulation and Experimental Validation

In order to validate the DFIG system impedance modeling, the SSR and HFR phenomena, as well as the active damping strategy for the HFR, the simulation results of a 2.0 MW commercial large-scale DFIG system and experimental results of a 7.5 kW small-scale DFIG system are provided.

A. Control Block Diagram

Fig. 42 shows the control block diagram of the proposed active damping strategy implemented through the feedforward control of rotor current or stator current in the RSC or through the feedforward control of grid current in the GSC. As it can be seen, for the RSC control, an enhanced phase-locked loop (EPLL) [6]–[10] is able to provide the information of grid voltage fundamental synchronous angular speed ω_1 and angle θ_1 information, while an encoder gives out the DFIG rotor position θ_r and speed ω_r. The rotor current $\boldsymbol{I}_{\mathrm{rdq}}^{+}$ is first sampled and then controlled based on the reference value $\boldsymbol{I}_{\mathrm{rdq}}^{+*}$ with a PI controller to output the harvested wind energy. The stator current $\boldsymbol{I}_{\mathrm{sdq}}^{+}$ or rotor current $\boldsymbol{I}_{\mathrm{rdq}}^{+}$ is also sampled for the feedforward control with the introduction of a virtual impedance.

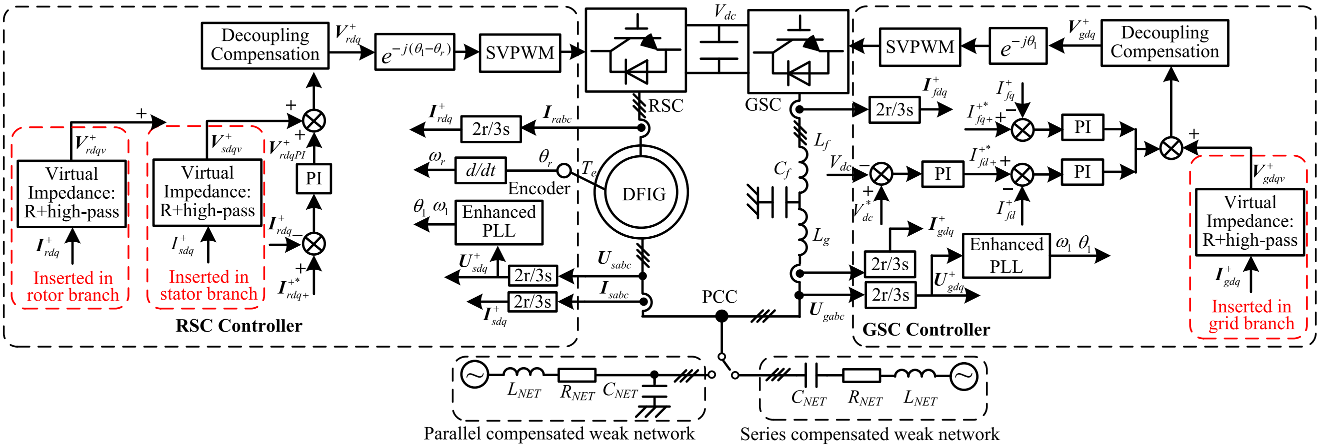

Fig. 42. Control block diagram of the DFIG system considering SSR and HFR, and the mitigation of HFR, the transformer is not included.

Note that according to Figs. 36, 39, and 41, the proposed active damping strategy is able to reduce the phase response of the DFIG system with a large frequency range, around 1000–2000 Hz. This means any potential HFR in the range of 1000–2000 Hz can all be mitigated, and no specific and accurate HFR frequency detection is required for the active damping. Instead, it is only needed to estimate the approximate HFR frequency (such as assume to be 1600 Hz in this paper) in order to calculate the virtual impedance parameter f_{cut} and R_v. Certain deviation of these two parameters has no significant influence on the active damping performance because sufficiently large phase margin can be produced, as shown in Figs. 36, 39, and 41, and a successful active damping can still be achieved.

Moreover, if the grid impedance changes due to the source and load switching, and as long as the potential HFR frequency remains within the range of 1000–2000 Hz, the proposed active damping strategy is still able to mitigate the HFR, meaning the predesigned parameters are still effective. However, if too large grid impedance change is seen and causes a large HFR frequency change, then the virtual impedance parameters have to be redesigned. This can be regarded as the limitation of the proposed active damping strategy.

It should be pointed out that the transformers are not shown in Fig. 42 for the sake of simplicity but have been included in the experimental and simulation results. The output of the rotor current PI closed-loop control $\boldsymbol{V}^+_{\mathrm{rdqPI}}$ and the output of virtual impedance resonance damping $\boldsymbol{V}^+_{\mathrm{sdqv}}$ or $\boldsymbol{V}^+_{\mathrm{rdqv}}$ are added, together with the decoupling compensation, giving out the rotor control voltage $\boldsymbol{V}^+_{\mathrm{rdq}}$, which is then transformed to the rotor stationary frame and delivered as the input to the space vector pulsewidth modulation (SVPWM).

As for the GSC control, the dc-link voltage V_{dc} is well regulated by a PI controller, and its output is delivered as the converter side inductance filter current reference $\boldsymbol{I}^{+*}_{\mathrm{fdq}}$, which is used to regulate the actual converter side inductance filter current $\boldsymbol{I}^+_{\mathrm{fdq}}$ by a PI controller. The grid side current $\boldsymbol{I}^+_{\mathrm{gdq}}$ is also sampled for the introduction of the virtual impedance in the grid part of the DFIG system, and its corresponding output is $\boldsymbol{V}^+_{\mathrm{gdqv}}$. The GSC control voltage $\boldsymbol{V}^+_{\mathrm{gdq}}$ can be obtained by the PI current controller output, the virtual impedance output $\boldsymbol{V}^+_{\mathrm{gdqv}}$, and the decoupling compensation unit.

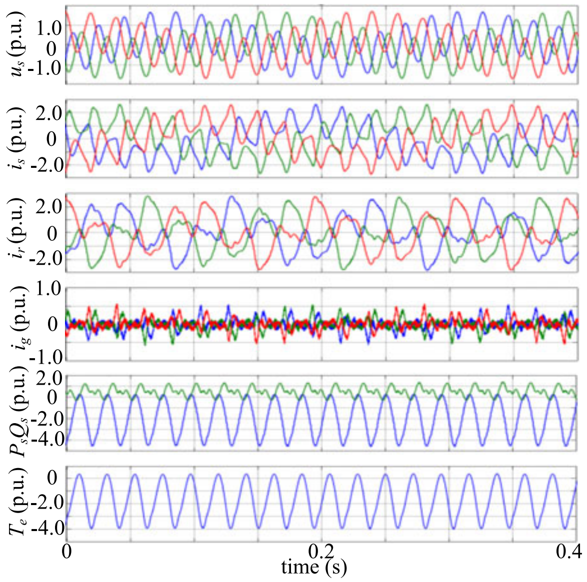

Fig. 43. Simulation of SSR in a small-scale DFIG system using the parameters in Table I, series compensated weak grid network with the parameters given in Table IV, i.e., $R_{\mathrm{NETS}} = 0.1$ mΩ, $L_{\mathrm{NETS}} = 0.01$ mH, $C_{\mathrm{NETS}} = 0.1$ F. Rotor speed = 0.8 p.u. DFIG stator voltage u_s, stator current i_s and rotor current i_r, and grid side current i_g, stator active and reactive power P_s and Q_s, and electromagnetic torque T_e.

B. SSR Validation in Both Small- and Large-Scale DFIG Systems

The SSR in both small- and large-scale DFIG systems is validated based on a simulation model in MATLAB Simulink.

Fig. 43 shows the simulation results of SSR in the small-scale DFIG system using the parameters given in Table I and the series compensated weak grid network using parameters in Table IV, i.e., $R_{\mathrm{NETS}} = 0.1$ mΩ, $L_{\mathrm{NETS}} = 0.01$ mH, $C_{\mathrm{NETS}} = 0.1$ F, and rotor speed = 0.8 p.u. As can be observed from Fig. 43, the small-scale DFIG system suffers from SSR, with the stator voltage and current u_s and i_s containing the resonance

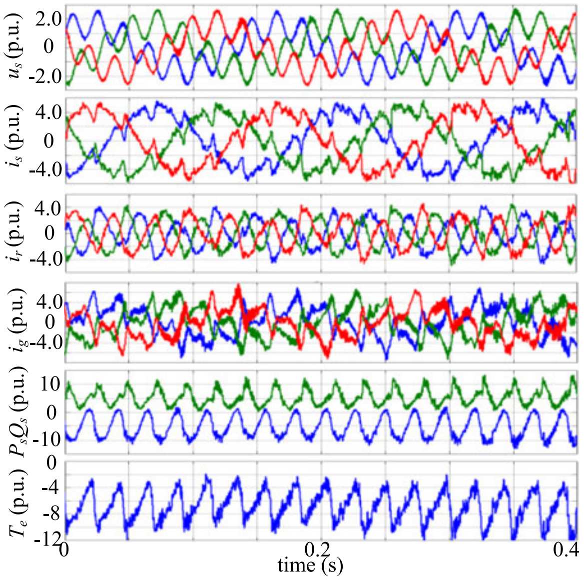

Fig. 44. Simulation of SSR in a large-scale DFIG system with parameter in Table II, series compensated weak grid network with the parameters given in Table IV, i.e., $R_{\mathrm{NETS}} = 0.3\ \Omega$, $L_{\mathrm{NETS}} = 3.93$ mH, $C_{\mathrm{NETS}} = 520\,\mu$F, and $K_3 = 25$. Rotor speed = 0.8 p.u. DFIG stator voltage u_s, stator current i_s and rotor current i_r, and grid side current i_g, stator active and reactive power P_s and Q_s, and electromagnetic torque T_e.

component of 4 Hz. This result matches well with the theoretical analysis result (SSR frequency = 5 Hz) in Fig. 16. Due to the interaction between the SSR component (4 Hz) and the fundamental component (50 Hz) in the stator current and voltage, the stator output active and reactive power P_s and Q_s contain the resonance component of 46 Hz. The same is true concerning the pulsation of the electromagnetic torque T_e. For the rotor current i_r, since the rotor speed is set to 0.8 p.u., the rotor current contains the resonance component of 4 Hz − 40 Hz = −36 Hz.

The simulation results of the large-scale DFIG system SSR is shown in Fig. 44 and the parameters of the large-scale DFIG system is available in Table II, rotor speed = 0.8 p.u. The parameters of the series compensated weak network are $R_{\mathrm{NETS}} = 0.3\ \Omega$, $L_{\mathrm{NETS}} = 3.93$ mH, and $C_{\mathrm{NETS}} = 520\,\mu$F; note that the voltage changing ratio $K_3 = 25$ also needs to be considered. Therefore, the actual values of the series compensated weak network seen from the PCC as shown in Fig. 1 can be calculated as, $R_{\mathrm{NETS}}/K_3^2 = 0.48$ mΩ, $L_{\mathrm{NETS}}/K_3^2 = 0.0063$ mH, $C_{\mathrm{NETS}} * K_3^2 = 0.325$ F. Similar to the results in Fig. 43, the large-scale DFIG system also suffers the SSR with the resonance frequency of 7.5 Hz. This simulation result also matches well the theoretical analysis of 5.8 Hz shown in Fig. 17.

Due to the interaction between the SSR component (7.5 Hz) and the fundamental component (50 Hz) in the stator current and voltage, the stator output active and reactive power P_s and Q_s, as well as the electromagnetic torque T_e contain the resonance component of 42.5 Hz, and the rotor current contains the resonance component of 7.5 Hz − 40 Hz = −32.5 Hz due to the rotor speed of 0.8 p.u (see Table V).

Furthermore, it should be pointed out that in the simulation results of both Figs. 43 and 44, the low-frequency SSR components of stator voltage u_s, stator current i_s, and rotor current i_r all have large amplitude, i.e., around 2.0 p.u., as shown in Fig. 43, and 4.0 p.u., as shown in Fig. 44; as a consequence, the output active and reactive power as well as the electromagnetic torque also contain large dc components due to the interaction between SSR components in the stator voltage and currents. Moreover, the large amplitude of the pulsation components of P_s, Q_s, and T_e in Figs. 43 and 44 are also similarly caused by the interaction between the large-amplitude SSR components and the fundamental components. This large pulsation components may not occur in practice due to the overvoltage and overcurrent trip in the DFIG protection unit, but here they are shown in simulation results for the purpose of better explaining the SSR phenomenon in the DFIG system.

TABLE V
THEORETICAL AND SIMULATION RESULTS OF SSR IN SMALL- AND LARGE-SCALE DFIG SYSTEMS

SSR Frequency	Small-Scale 7.5 kW	Large-Scale 2.0 MW
Theoretical result	5 Hz	5.8 Hz
Simulation result	4 Hz	7.5 Hz

TABLE VI
THEORETICAL AND SIMULATION RESULTS OF HFR IN SMALL- AND LARGE-SCALE DFIG SYSTEMS

HFR Frequency	Small Scale	Large Scale
Theoretical result	1575 Hz	1385 Hz
Experimental result	1600 Hz	
Simulation result		1520 Hz

C. HFR Validation and Active Damping in the Small-Scale DFIG System

The HFR validation is conducted based on experiments of a small-scale DFIG system and simulations of a large-scale DFIG system. The parameters of the small- and the large-scale DFIG are listed in Tables I and II, and the parameters of the parallel compensated weak network are listed in Table III.

In order to experimentally validate the DFIG system impedance modeling and the HFR behavior, a downscaled 7.5 kW test rig is built up and shown in Fig. 45, with its parameters given in Table I. The DFIG is externally driven by a prime motor, and two 5.5-kW Danfoss motor drives are used for the GSC and the RSC, both of which are controlled with dSPACE 1006 control system. The rotor speed is set to 1200 r/min (0.8 p.u.), the dc-link voltage is 650 V. The DFIG stator output active and reactive power are set to 5 kW and 0 Var, respectively. The sampling and switching frequency of both converters are 10 and 5 kHz, respectively.

It should be pointed out that the experiment validation is conducted under the weak network parameters of $R_{\mathrm{NET}} = 3$mΩ, $L_{\mathrm{NET}} = 1.5$ mH, and $C_{\mathrm{NET}} = 10\,\mu$F. These weak network parameters are different from the theoretical analysis part, and the Bode diagrams of this weak grid impedance and the small-scale

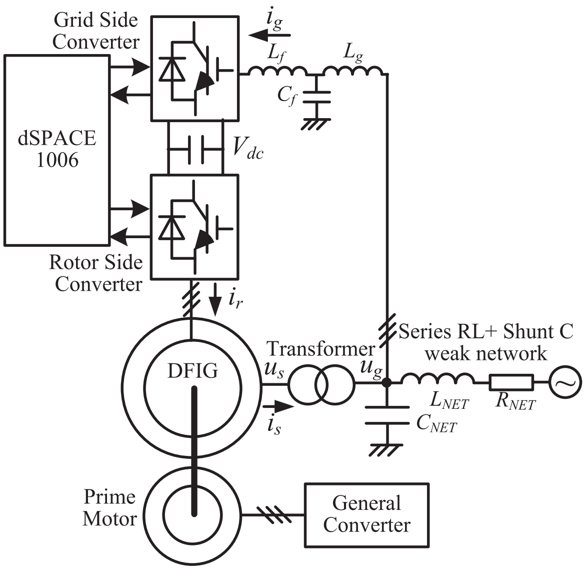

Fig. 45. Setup of a 7.5 kW DFIG system test rig.

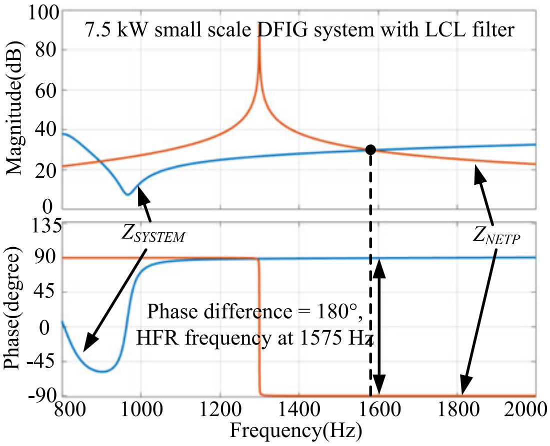

Fig. 46. Bode diagram of the small-scale DFIG system impedance and the parallel compensated weak network impedance with $C_{\mathrm{NET}} = 10\,\mu$F, $R_{\mathrm{NET}} = 3$ mΩ, and $L_{\mathrm{NET}} = 1.5$ mH.

DFIG system have been plotted in Fig. 46. As it can be seen, the theoretical analysis shows that the HFR will occur at 1575 Hz.

Fig. 47 shows the experimental results of the small-scale DFIG system, when the rotor speed is 1200 r/min (0.8 p.u. below the synchronous speed), the weak grid network $R_{\mathrm{NET}} = 3$ mΩ, $L_{\mathrm{NET}} = 1.5$ mH, and $C_{\mathrm{NET}} = 10\,\mu$F. Obviously, due to the impedance interaction between the small-scale DFIG system and the parallel compensated network, the HFR occurs, and the stator voltage u_s, the stator current i_s, the rotor current i_r, the grid voltage u_g, and the grid side current i_g all contain high-frequency HFR components. The resonance frequency in the experimental results can be analyzed to be 1600 Hz. It can be seen that the resonance frequency in the experimental results match well with the theoretical analysis within an acceptable error (see Table VI). The error can be attributed to the DFIG system parameters deviation due to temperature changing, skin effect, and flux saturation and also because of the deviation of the weak network parameters.

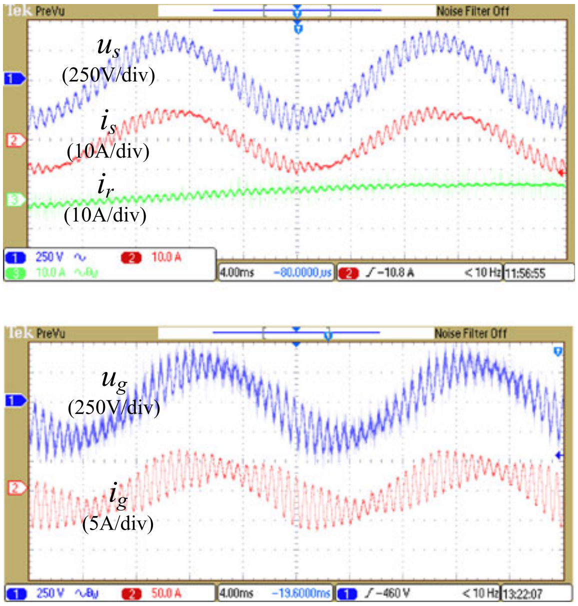

Fig. 47. Experimental result of the HFR in the small-scale DFIG system when the active damping strategy is disabled.

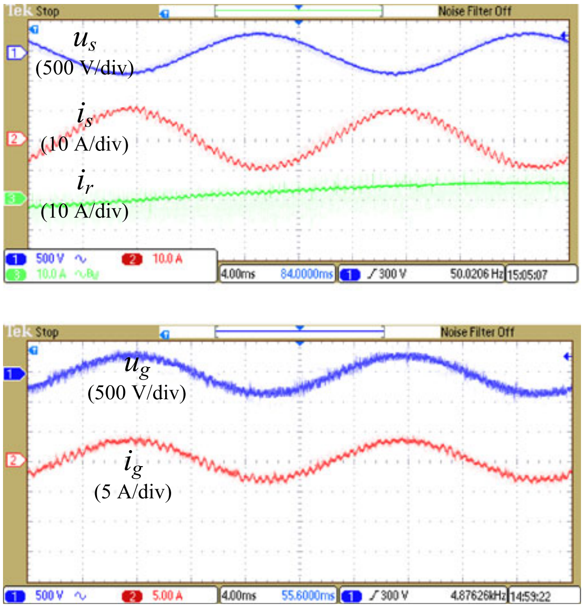

Fig. 48. Experimental result of the HFR in the small-scale DFIG system when the active damping strategy is enabled.

Fig. 48 shows the experimental results of the small-scale DFIG system when an active damping strategy is enabled. Note that the virtual impedance inserted in the stator part is taken as an example, while the other two methods that insert a virtual impedance in the rotor and grid part have similar performance and will not be described here. Obviously, the HFR resonance components in Fig. 47 can be effectively mitigated when the active damping strategy is enabled, and as a result, the resonance components in the stator voltage and current and grid

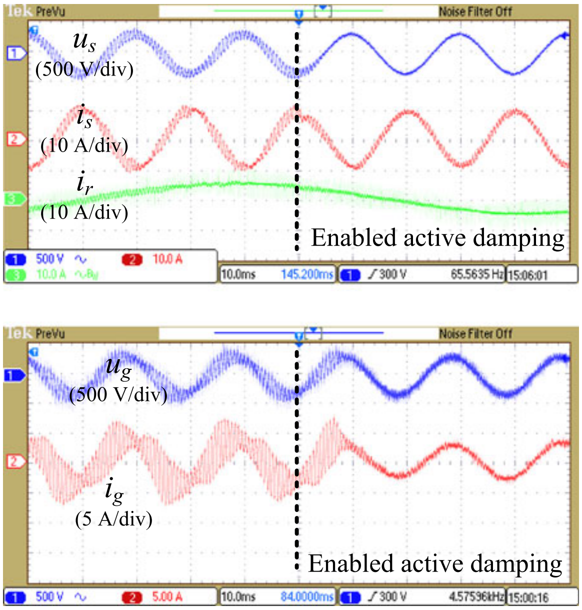

Fig. 49. Experimental result of the HFR damping transient response in the small-scale DFIG system when the active damping strategy is enabled.

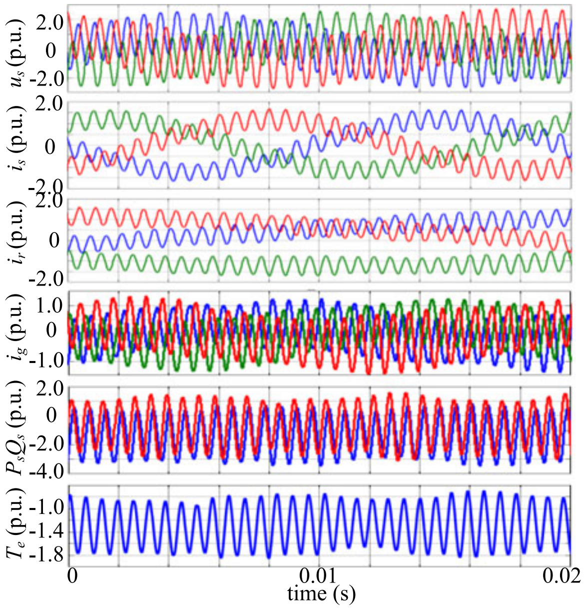

Fig. 50. Simulation results of a 2.0 MW large-scale DFIG system HFR when active damping is disabled, parallel compensated weak grid network $R_{\mathrm{NETP}} = 10.3\ \Omega$, $L_{\mathrm{NETP}} = 36.6$ mH, $C_{\mathrm{NETP}} = 1.02\,\mu$F, and $K_3 = 25$. DFIG stator voltage u_s, stator current i_s and rotor current i_r, grid side current i_g, stator active and reactive power P_s and Q_s, and electromagnetic torque T_e.

side voltage and current become much smaller. Therefore, the effectiveness of the proposed active damping strategy in the small-scale DFIG system can be validated.

Fig. 49 shows the experimental result of the transient response of DFIG system when the active damping strategy is enabled. Once enabled, the active damping strategy is capable of mitigating the HFR components within 10 ms in the stator voltage and current, as well as the grid side voltage and current. This experimental result verifies a good dynamic performance of the proposed active damping strategy in the small-scale DFIG system.

D. HFR Validation and Active Damping in the Large-Scale DFIG System

In order to validate the HFR in the large-scale DFIG system, simulations are provided based on MATLAB Simulink. The simulation of a 2.0-MW large-scale DFIG system HFR is conducted with the parallel compensated weak network parameters given in Table III. According to Table III, the parameters of the parallel compensated weak network for the large-scale DFIG system are $R_{\mathrm{NETP}} = 10.3\ \Omega$, $L_{\mathrm{NETP}} = 36.6$ mH, and $C_{\mathrm{NET}} = 1.02\,\mu$F; note that the voltage changing ratio $K_3 = 25$ also needs to be considered. Therefore, the actual values of the parallel compensated weak network seen from the PCC, as shown in Fig. 1, can be calculated as, $R_{\mathrm{NETP}}/K_3^2 = 16$ mΩ, $L_{\mathrm{NETP}}/K_3^2 = 0.058$ mH, and $C_{\mathrm{NETP}} * K_3^2 = 637\,\mu$F. Moreover, it needs to be pointed out that the large parallel network inductance $L_{\mathrm{NETP}} = 36.6$ mH is possible due to the parasitic inductance of the high-voltage long-distance transmission cables. As shown in Fig. 19, the theoretical analysis result of HFR in the large-scale DFIG system is 1385 Hz. During the simulations, the DFIG system output active power is 1.0 p.u., reactive power is 0 p.u., and the rotor speed is 0.8 p.u. below synchronous speed.

As it can be seen from Fig. 50, when the 2.0 MW DFIG system is connected to the parallel compensated network, the HFR at 1520 Hz occurs in the stator voltage, the stator/rotor current, and the grid side current. Besides, due to the resonance components in the voltage and current, the stator output active and reactive power P_s and Q_s, as well as the electromagnetic torque T_e include also the HFR components. It can be found that the simulation result of 1520 Hz matches with the theoretical result of 1385 Hz with an acceptable frequency error (see Table VI). Thus, the HFR analysis in the large-scale DFIG system can be verified.

Fig. 51 shows the simulation results when the active damping strategy is enabled, the virtual impedance is inserted in the stator part. The other two methods that insert the virtual impedance in the rotor and grid part have similar performance and will not be described here.

By comparing the simulation results in Figs. 50 and 51, it can be clearly observed that the HFR resonance components in Fig. 50 can be well mitigated. The stator voltage, stator and rotor current are able to operate with sinusoidal waveforms, and the fluctuation in the stator output power and electromagnetic torque can be eliminated. Thus, the effectiveness of the proposed active damping strategy in the large-scale DFIG system can be verified.

Fig. 52 shows the simulation results of the transient response at the enabling instant of the active damping strategy. By comparing the DFIG system performance before and after the enabling instant, the effectiveness of the proposed active damping strategy can be verified again. Moreover, the transient response takes around 500 ms to achieve the damping, which is acceptable for a large-scale DFIG system. The stator output active and

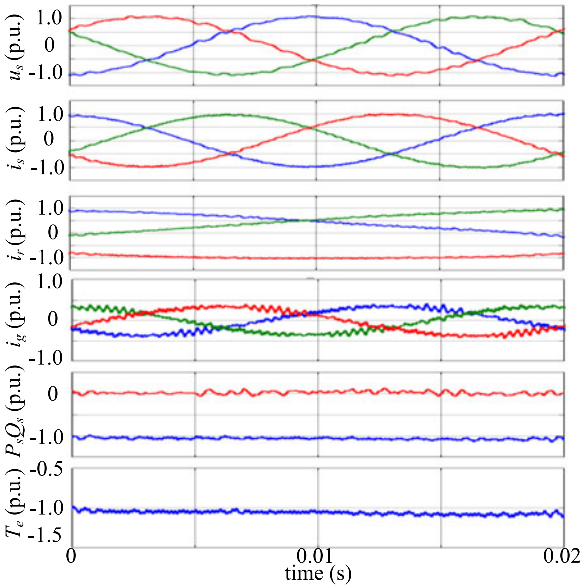

Fig. 51. Simulation results of 2.0 MW large-scale DFIG system HFR when active damping is enabled, weak grid network $R_{\mathrm{NETP}} = 10.3\ \Omega$, $L_{\mathrm{NETP}} = 36.6$ mH, $C_{\mathrm{NETP}} = 1.02\ \mu$F, $K_3 = 25$. DFIG stator voltage u_s, stator current i_s and rotor current i_r, and grid side current i_g, stator active and reactive power P_s and Q_s, and electromagnetic torque T_e.

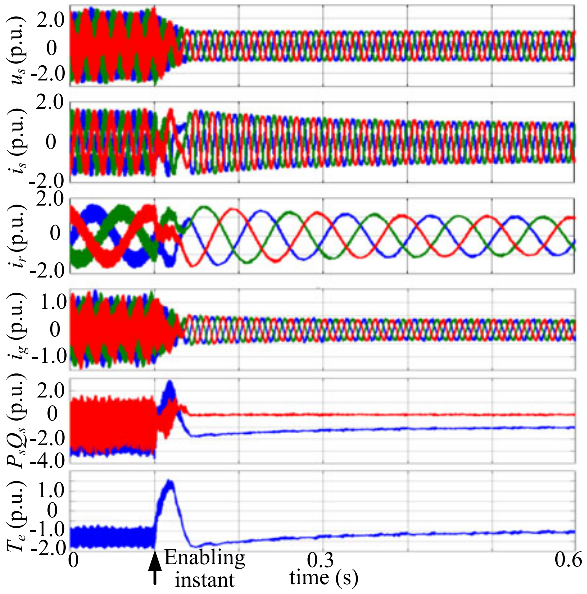

Fig. 52. Simulation results of 2.0 MW large-scale DFIG system HFR transient response when active damping is enabled, weak grid network $R_{\mathrm{NET}} = 10.3\ \Omega$, $L_{\mathrm{NET}} = 36.6$ mH, $C_{\mathrm{NET}} = 1.02\ \mu$F, $K_3 = 25$. DFIG stator voltage u_s, stator current i_s and rotor current i_r, and grid side current i_g, stator active and reactive power P_s and Q_s, and electromagnetic torque T_e.

reactive power can still be accurately regulated when the active damping strategy is enabled, which makes this strategy more practical and reliable in practice.

VII. CONCLUSION

This overview paper discusses the SSR and HFR phenomena in the small- and large-scale DFIG systems when connected to the series and parallel compensated weak network. The main contributions and conclusions can be summarized as follows:

1) The impedance modeling of the DFIG system, including the DFIG machine and RSC and the GSC and output filter, is established. During the modeling, GSCs with *L* or *LCL* filter are considered and the digital control delay is also taken into consideration. The impedance modeling of noncompensated, series compensated, and parallel compensated weak networks are established. Based on the earlier impedance modeling, the SSR and HFR of both small- and large-scale DFIG systems can be analyzed and identified.
2) During the SSR and HFR analysis, the following several factors are considered: a) transformer configuration; b) different power-scale DFIG system with different parameters; c) *L* or *LCL* filter adopted in GSC; d) rotor speed; e) current closed-loop control proportional and integral parameters; and f) digital control delay.
3) It has been proved that the transformer configuration has obvious influence on the impedance shape of the DFIG system and the weak network; thus, the SSR and HFR can be affected. The DFIG system with a different power scale has also quite different impedance shape due to significantly different parameters. The rotor speed and current control parameters are relevant to the DFIG system SSR phenomenon but is relatively not important to the DFIG system HFR phenomenon.
4) The active damping strategy for HFR is able to appropriately reshape the impedance of DFIG system by inserting the virtual impedance (which consists of virtual positive resistance, high-pass filter, and digital control delay) in the grid part, rotor part, and stator part of the DFIG system; thus, the HFR can be effectively mitigated by reducing the phase difference between the DFIG system and the parallel compensated weak network to a smaller value than 180°.

REFERENCES

[1] F. Blaabjerg and K. Ma, "Future on power electronics for wind turbine systems," *IEEE J. Emer. Sel. Topics Power Electron.*, vol. 1, no. 3, pp. 139–152, Sep. 2013.
[2] K. Ma, L. Tutelea, I. Boldea, D. M. Ionel, and F. Blaabjerg, "Power electronic drives, controls, and electric generators for large wind turbines—An overview," *Electric Power Compon. Syst.*, vol. 43, no. 12, pp. 1406–1421, 2015.
[3] V. Yaramasu, B. Wu, P. C. Sen, S. Kouro, and M. Narimani, "High-power wind energy conversion systems: State-of-the-art and emerging technologies," *Proc. IEEE*, vol. 103, no. 5, pp. 740–788, May 2015.
[4] Z. Chen, J. M. Guerrero, and F. Blaabjerg, "A review of the state of the art of power electronics for wind turbines," *IEEE Trans. Power Electron.*, vol. 24, no. 8, pp. 1859–1875, Aug. 2009.
[5] X. Wang, F. Blaabjerg, and P. C. Loh, "Proportional derivative based stabilizing control of paralleled grid converters with cables in renewable power plants," in *Proc. Energy Convers. Congr. Expo.*, 2014, pp. 4917–4924.
[6] H. Nian, P. Cheng, and Z. Q. Zhu, "Independent operation of DFIG-based WECS using resonant feedback compensators under unbalanced grid voltage conditions," *IEEE Trans. Power Electron.*, vol. 30, no. 7, pp. 3650–3661, Jul. 2015.
[7] H. Nian, P. Cheng, and Z. Q. Zhu, "Coordinated direct power control of DFIG system without phase-locked loop under unbalanced grid voltage conditions," *IEEE Trans. Power Electron.*, vol. 31, no. 4, pp. 2905–2918, Apr. 2016.

[8] P. Cheng and H. Nian, "Collaborative control of DFIG system during network unbalance using reduced-order generalized integrators," *IEEE Trans. Energy Convers.*, vol. 30, no. 2, pp. 453–464, Jun. 2015.

[9] P. Cheng, H. Nian, C. Wu, and Z. Q. Zhu, "Direct stator current vector control strategy of DFIG without phase locked loop during network unbalance," *IEEE Trans. Power Electron.*, Early Access.

[10] H. Nian, Y. Song, P. Zhou, and Y. He, "Improved direct power control of a wind turbine driven doubly fed induction generator during transient grid voltage unbalance," *IEEE Trans. Energy Convers.*, vol. 26, no. 3, pp. 976–986, Sep. 2011.

[11] D. Zhou, F. Blaabjerg, T. Franke, M. Lau, and M. Tonnes, "Reduced cost of reactive power in doubly fed induction generator wind turbine system with optimized grid filter," *IEEE Trans. Power Electron.*, vol. 30, no. 10, pp. 5581–5590, Oct. 2015.

[12] D. Zhou, F. Blaabjerg, T. Franke, M. Tonnes, and M. Lau, "Optimized reactive power flow of DFIG power converters for better reliability performance considering grid codes," *IEEE Trans. Ind. Electron.*, vol. 62, no. 3, pp. 1552–1562, Mar. 2015.

[13] R. Zhu, Z. Chen, Y. Tang, F. Deng, and X Wu, "Dual-loop control strategy for DFIG-based wind turbines under grid voltage disturbances," *IEEE Trans. Power Electron.*, vol. 31, no. 3, pp. 2239–2253, Mar. 2016.

[14] W. Chen, F. Blaabjerg, N. Zhu, M. Chen, and D. Xu, "Doubly fed induction generator wind turbine systems subject to recurring symmetrical grid faults," *IEEE Trans. Power Electron.*, vol. 31, no. 2, pp. 1143–1160, Feb. 2016.

[15] Y. Song and H. Nian, "Modularized control strategy and performance analysis of DFIG system under unbalanced and harmonic grid voltage," *IEEE Trans. Power Electron.*, vol. 30, no. 9, pp. 4831–4842, Sep. 2015.

[16] H. Nian and Y. Song, "Direct power control of doubly fed induction generator under distorted grid voltage," *IEEE Trans. Power Electron.*, vol. 29, no. 2, pp. 894–905, Feb. 2014.

[17] Y. Song and H. Nian, "Enhanced grid-connected operation of DFIG using improved repetitive control under generalized harmonic power grid," *IEEE Trans. Energy Convers.*, vol. 30, no. 3, pp. 1019–1029, Sep. 2015.

[18] Y. Song and H. Nian, "Sinusoidal output current implementation of DFIG using repetitive control under a generalized harmonic power grid with frequency deviation," *IEEE Trans. Power Electron.*, vol. 30, no. 12, pp. 6751–6762, Dec. 2015.

[19] K. Kim, Y. Jeung, D. Lee, and H. Kim, "LVRT scheme of PMSG wind power systems based on feedback linearization," *IEEE Trans. Power Electron.*, vol. 27, no. 5, pp. 2376–2384, May 2015.

[20] M. Fatu, F. Blaabjerg, and I. Boldea, "Grid to standalone transition motion-sensorless dual-inverter control of PMSG with asymmetrical grid voltage sags and harmonics filtering," *IEEE Trans. Power Electron.*, vol. 29, no. 7, pp. 3463–3472, Jul. 2014.

[21] S. Li, T. Haskew, R. Swatloski, and W. Gathings, "Optimal and direct-current vector control of direct-driven PMSG wind turbines," *IEEE Trans. Power Electron.*, vol. 27, no. 5, pp. 2325–2337, May 2012.

[22] Y. Wang, J. Meng, X. Zhang, and L. Xu, "Control of PMSG-based wind turbines for system inertial response and power oscillation damping," *IEEE Trans. Sustain. Energy*, vol. 6, no. 2, pp. 565–574, Apr. 2015.

[23] J. Dai, D. Xu, and B. Wu, "A novel control scheme for current-source converter-based PMSG wind energy conversion systems," *IEEE Trans. Power Electron.*, vol. 24, no. 4, pp. 963–972, Apr. 2009.

[24] A. Rajaei, M. Mohamadian, and A. Varjani, "Vienna-rectifier-based direct torque control of PMSG for wind energy application," *IEEE Trans. Ind. Electron.*, vol. 60, no. 7, pp. 2919–2929, Jul. 2013.

[25] K. Tan, "Squirrel-cage induction generator system using wavelet petri fuzzy neural network control for wind power applications," *IEEE Trans. Power Electron.*, vol. 31, no. 7, pp. 5242–5254, Jul. 2016.

[26] Y. Song, X. Wang, and F. Blaabjerg, "High frequency resonance damping of DFIG based wind power system under weak network," *IEEE Trans. Power Electron.*, Early Access.

[27] Y. Song, X. Wang, and F. Blaabjerg, "Impedance-based super-synchronous resonance analysis of DFIG system in weak grids," *IEEE Trans. Power Electron.*, Early Access.

[28] Y. Song and F. Blaabjerg, "Wide frequency band active damping strategy for DFIG system high frequency resonance," *IEEE Trans. Energy. Convers.*, Early Access.

[29] I. Vieto and J. Sun, "Small-signal impedance modeling of type-III wind turbine," in *Proc. Power Energy Soc. General Meeting*, 2015, pp. 1–5.

[30] I. Vieto and J. Sun, "Real-time simulation of subsynchronous resonance in type-III wind turbines," in *Proc. Control Modeling Power Electron.*, 2014, pp. 1–8.

[31] Z. Miao, "Impedance-model-based SSR analysis for type 3 wind generator and series-compensated network," *IEEE Trans. Energy Convers.*, vol. 27, no. 4, pp. 984–991, Dec. 2012.

[32] L. Piyasinghe, Z. Miao, J. Khazaei, and L. Fan, "Impedance model-based SSR analysis for TCSC compensated type-3 wind energy delivery systems," *IEEE Trans. Sustain. Energy*, vol. 6, no. 1, pp. 179–187, Jan. 2015.

[33] H. A. Mohammadpour, Y. Shin, and E. Santi, "SSR analysis of a DFIG-based wind farm interfaced with a gate-controlled series capacitor," in *Proc. Appl. Power Electron. Conf. Expo.*, 2014, pp. 3110–3117.

[34] L. Fan and Z. Miao, "Nyquist-stability-criterion-based SSR explanation for type-3 wind generators," *IEEE Trans. Energy Convers.*, vol. 27, no. 3, pp. 807–809, Sep. 2012.

[35] L. Wang, X. Xie, Q. Jiang, H. Liu, Y. Li, and H. Liu, "Investigation of SSR in practical DFIG-based wind farms connected to a series-compensated power system," *IEEE Trans. Power Syst.*, vol. 30, no. 5, pp. 2772–2779, Sep. 2015.

[36] L. Fan, R. Kavasseri, Z. Miao, and C. Zhu, "Modeling of DFIG-based wind farms for SSR analysis," *IEEE Trans. Power Del.*, vol. 25, no. 4, pp. 2073–2082, Oct. 2010.

[37] H. Liu, X. Xie, C. Zhang, Y. Li, H. Liu, and Y. Hu, "Quantitative SSR analysis of series-compensated DFIG-based wind farms using aggregated RLC circuit model," *IEEE Trans. Power Syst.*, Early Access.

[38] L. Fan, C. Zhu, Z. Miao, and M. Hu, "Modal analysis of a DFIG-based wind farm interfaced with a series compensated network," *IEEE Trans. Energy Convers.*, vol. 26, no. 4, pp. 1010–1020, Dec. 2011.

[39] H. A. Mohammadpour and E. Santi, "Sub-synchronous resonance analysis in DFIG-based wind farms: Definitions and problem identification—Part I," in *Proc. IEEE Energy Convers. Congr. Expo.*, Sep. 2014, pp. 812–819.

[40] I. Vieto and J. Sun, "Damping of subsynchronous resonance involving type-III wind turbines," in *Proc. Control Modeling Power Electron.*, 2015. pp. 1–8.

[41] L. Fan and Z. Miao, "Mitigating SSR using DFIG-based wind generation," *IEEE Trans. Sustain. Energy*, vol. 3, no. 3, pp. 349–358, Jul. 2012.

[42] H. A. Mohammadpour and E. Santi, "SSR damping controller design and optimal placement in rotor-side and grid-side converters of series-compensated DFIG-based wind farm," *IEEE Trans. Sustain. Energy*, vol. 6, no. 2, pp. 388–399, Apr. 2015.

[43] A. E. Leon and J. A. Solsona, "Sub-synchronous interaction damping control for DFIG wind turbines," *IEEE Trans. Power Syst.* vol. 30, no. 1, pp. 419–428, Jan. 2015.

[44] P. Huang, M. Moursi, W. Xiao, and J. Kirtley, "Subsynchronous resonance mitigation for series-compensated DFIG-based wind farm by using two-degree-of-freedom control strategy," *IEEE Trans. Power Syst.*, vol. 30, no. 3, pp. 1442–1454, May 2015.

[45] A. Leon, "Integration of DFIG-based wind farms into series-compensated transmission systems," *IEEE Trans. Sustain. Energy*, vol. 7, no. 2, pp. 451–460, Apr. 2016.

[46] H. A. Mohammadpour and E. Santi, "Sub-synchronous resonance analysis in DFIG-based wind farms: Mitigation methods—TCSC, GCSC, and DFIG controllers—Part II," in *Proc. IEEE Energy Convers. Congr. Expo.*, Sep. 2014, pp. 1550–1557.

[47] X. Wang, F. Blaabjerg, and P. C. Loh, "Grid-current-feedback active damping for *LCL* resonance in grid-connected voltage source converters," *IEEE Trans. Power Electron.*, vol. 31, no. 1, pp. 213–223, Jan. 2016.

[48] X. Wang, F. Blaabjerg, and P. C. Loh, "Virtual RC damping of *LCL*-filtered voltage source converters with extended selective harmonic compensation," *IEEE Trans. Power Electron.*, vol. 30, no. 9, pp. 4726–4737, Sep. 2015.

[49] X. Wang, F. Blaabjerg, and W. Wu, "Modeling and analysis of harmonic stability in an AC power-electronics-based power system," *IEEE Trans. Power Electron.*, vol. 29, no. 12, pp. 6421–6432, Dec. 2014.

[50] X. Wang, F. Blaabjerg, M. Liserre, Z. Chen, J. He, and Y. Li, "An active damper for stabilizing power-electronics-based AC systems," *IEEE Trans. Power Electron.*, vol. 29, no. 7, pp. 3318–3329, Jul. 2014.

[51] X. Wang, Y. Li, F. Blaabjerg, and P. C. Loh, "Virtual-impedance-based control for voltage-source and current-source converters," *IEEE Trans. Power Electron.*, vol. 30, no. 12, pp. 7019–7037, Dec. 2015.

[52] C. Wan, M. Huang, C. K. Tse, and X. Ruan, "Effects of interaction of power converters coupled via power grid: A design-oriented study," *IEEE Trans. Power Electron.*, vol. 30, no. 7, pp. 3589–3600, Jul. 2015.

[53] X. Wang, C. Bao, X. Ruan, W. Li, and D. Pan, "Design considerations of digitally controlled *LCL*-filtered inverter with capacitor current-feedback active damping," *IEEE J. Emer. Sel. Topics Power Electron.*, vol. 2, no. 4, pp. 972–984, Dec. 2014.

[54] C. Bao, X. Ruan, X. Wang, W. Li, D. Pan, and K. Weng, "Step-by-step controller design for *LCL*-type grid-connected inverter with capacitor–current-feedback active-damping," *IEEE Trans. Power Electron.*, vol. 29, no. 3, pp. 1239–1253, Mar. 2014.

[55] D. Pan, X. Ruan, C. Bao, W. Li, and X. Wang, "Optimized controller design for *LCL*-type grid-connected inverter to achieve high robustness against grid-impedance variation," *IEEE Trans. Ind. Electron.*, vol. 62, no. 3, pp. 1537–1547, Mar. 2015.

[56] D. Pan, X. Ruan, C. Bao, W. Li, and X. Wang, "Capacitor-current-feedback active damping with reduced computation delay for improving robustness of *LCL*-type grid-connected inverter," *IEEE Trans. Power Electron.*, vol. 29, no. 7, pp. 3414–3427, Jul. 2014.

[57] D. Yang, X. Ruan, and H. Wu, "A real-time computation method with dual sampling mode to improve the current control performance of the *LCL*-type grid-connected inverter," *IEEE Trans. Ind. Electron.*, vol. 62, no. 7, pp. 4563–4572, Jul. 2015.

[58] D. Yang, X. Ruan, and H. Wu, "Impedance shaping of the grid-connected inverter with *LCL* filter to improve its adaptability to the weak grid condition," *IEEE Trans. Power Electron.*, vol. 29, no. 11, pp. 5795–5805, Nov. 2014.

[59] B. Wen, D. Boroyevich, R. Burgos, P. Mattavelli, and Z. Shen, "Analysis of D-Q small-signal impedance of grid-tied inverters," *IEEE Trans. Power Electron.*, vol. 31, no. 1, pp. 675–687, Jan. 2016.

[60] B. Wen, D. Boroyevich, R. Burgos, P. Mattavelli, and Z. Shen, "Small-signal stability analysis of three-phase AC systems in the presence of constant power loads based on measured d-q frame impedances," *IEEE Trans. Power Electron.*, vol. 30, no. 10, pp. 5952–5963, Oct. 2015.

[61] B. Wen, D. Dong, D. Boroyevich, R. Burgos, P. Mattavelli, and Z. Shen, "Impedance-based analysis of grid-synchronization stability for three-phase paralleled converters," *IEEE Trans. Power Electron.*, vol. 31, no. 1, pp. 26–38, Jan. 2016.

[62] B. Wen, D. Boroyevich, R. Burgos, P. Mattavelli, and Z. Shen, "Inverse Nyquist stability criterion for grid-tied inverters," *IEEE Trans. Power Electron.*, Early Access.

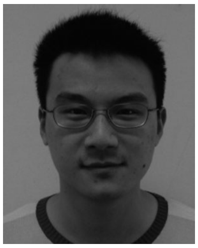

Yipeng Song (M'16) was born in Hangzhou, China. He received the B.Sc. degree and the Ph.D. degree both from the College of Electrical Engineering, Zhejiang University, Hangzhou, China, in 2010 and 2015, respectively.

He is currently a Postdoctoral Researcher in the Department of Energy Technology, Aalborg University, Aalborg, Denmark. His current research interests include motor control with power electronics devices in renewable energy conversion, particularly the control and operation of doubly fed induction generators for wind power generation.

Frede Blaabjerg (S'86–M'88–SM'97–F'03) received the Ph.D. degree from Aalborg University, Aalborg, Denmark, in 1992.

He was with ABB-Scandia, Randers, Denmark, from 1987 to 1988. He became an Assistant Professor at Aalborg University in 1992, an Associate Professor in 1996, and a Full Professor of Power Electronics and Drives in 1998. His current research interests include power electronics and its applications such as in wind turbines, PV systems, reliability, harmonics, and adjustable speed drives.

Dr. Blaabjerg has received 17 IEEE Prize Paper Awards, the IEEE PELS Distinguished Service Award in 2009, the EPE-PEMC Council Award in 2010, the IEEE William E. Newell Power Electronics Award 2014, and the Villum Kann Rasmussen Research Award 2014. He was an Editor-in-Chief of the IEEE TRANSACTIONS ON POWER ELECTRONICS from 2006 to 2012. He was nominated in 2014 and 2015 by Thomson Reuters to be between the most 250 cited researchers in engineering in the world.